Monthly Notices of the ROYAL ASTRONOMICAL SOCIETY

MNRAS **530,** 1984–2000 (2024) https://doi.org/10.1093/mnras/stae921
Advance Access publication 2024 April 24

A *JWST* investigation into the bar fraction at redshifts $1 \leq z \leq 3$

Zoe A. Le Conte,[1]★ Dimitri A. Gadotti [1]★ Leonardo Ferreira [2] Christopher J. Conselice,[3] Camila de Sá-Freitas [4] Taehyun Kim,[5] Justus Neumann [6] Francesca Fragkoudi,[7] E. Athanassoula[8] and Nathan J. Adams [3]

[1]*Centre for Extragalactic Astronomy, Department of Physics, Durham University, South Road, Durham DH1 3LE, UK*
[2]*Department of Physics and Astronomy, University of Victoria, Finnerty Road, Victoria, British Columbia V8P 1A1, Canada*
[3]*Jodrell Bank Centre for Astrophysics, University of Manchester, Oxford Road, Manchester M13 9PL, UK*
[4]*European Southern Observatory, Karl-Schwarzschild-Str. 2, D-85748 Garching bei Muenchen, Germany*
[5]*Department of Astronomy and Atmospheric Sciences, Kyungpook National University, Daegu 41566, Republic of Korea*
[6]*Max-Planck-Institut für Astronomie, Königstuhl 17, D-69117 Heidelberg, Germany*
[7]*Institute for Computational Cosmology, Department of Physics, Durham University, South Road, Durham DH1 3LE, UK*
[8]*LAM, CNRS, Aix Marseille Université, CNES, 13388 Marseille Cedex 13, France*

Accepted 2024 March 28. Received 2024 March 27; in original form 2023 September 18

ABSTRACT

The presence of a stellar bar in a disc galaxy indicates that the galaxy hosts in its main part a dynamically settled disc and that bar-driven processes are taking place in shaping its evolution. Studying the cosmic evolution of the bar fraction in disc galaxies is therefore essential to understand galaxy evolution in general. Previous studies have found, using the *Hubble Space Telescope* (*HST*), that the bar fraction significantly declines from the local Universe to redshifts near one. Using the first four pointings from the *JWST* Cosmic Evolution Early Release Science Survey and the initial public observations for the Public Release Imaging for Extragalactic Research, we extend the studies of the bar fraction in disc galaxies to redshifts $1 \leq z \leq 3$, that is, for the first time beyond redshift two. We only use galaxies that are also present in the Cosmic Assembly Near-IR Deep Extragalactic Legacy Survey on the Extended Groth Strip and Ultra Deep Survey *HST* observations. An optimized sample of 368 close-to-face-on galaxies is visually classified to find the fraction of bars in disc galaxies in two redshift bins: $1 \leq z \leq 2$ and $2 < z \leq 3$. The bar fraction decreases from $\approx 17.8^{+5.1}_{-4.8}$ per cent to $\approx 13.8^{+6.5}_{-5.8}$ per cent (from the lower to the higher redshift bin), but is about twice the bar fraction found using bluer *HST* filters. Our results show that bar-driven evolution might commence at early cosmic times and that dynamically settled discs are already present at a lookback time of ∼11 Gyr.

Key words: galaxies: bar – galaxies: disc – galaxies: distances and redshifts – galaxies: evolution – galaxies: general – galaxies: high-redshift.

1 INTRODUCTION

Stellar bars are one of the most abundant features in local disc galaxies (e.g. Eskridge et al. 2000; Marinova & Jogee 2007; Aguerri, Méndez-Abreu & Corsini 2009; Buta et al. 2015), providing insight into the internal evolutionary processes taking place in these galaxies. Several investigations using optical surveys in the local Universe find strong stellar bars in about a third of disc galaxies (e.g. Barazza et al. 2009; Nair & Abraham 2010; Masters et al. 2011). This fraction increases to 60 per cent–80 per cent if weaker bars are included (e.g. de Vaucouleurs et al. 1991; Méndez-Delmestre et al. 2007; Sheth et al. 2008; Erwin 2018).

Barred stellar structures in disc galaxies are thought to form relatively quickly, over times of the order of a hundred million years, in massive disc galaxies which are dynamically cold and rotationally supported (e.g. Hohl 1971; Kalnajs 1972; Ostriker & Peebles 1973; Sellwood & Wilkinson 1993). Hence, the formation of stellar bars is an indicator of the evolutionary stage of a galaxy. The bar is a dense central region of evolved stellar populations on highly eccentric orbits (e.g. Weinberg 1985; Contopoulos & Grosbol 1989; Athanassoula 1992; Kormendy & Kennicutt 2004). The non-axisymmetric nature of stellar bars is due to the very elongated form of the orbits that constitute the bar, which would be the x_1 orbital family or one of the higher multiplicity families, both parallel to the semimajor axis of the bar (Contopoulos & Papayannopoulos 1980; Wang et al. 2022), which have such properties. The orbital composition of the bar, coupled with the fact that the bar can be viewed from all possible angles, introduces a range of observed ellipticities. Therefore, the shape of the stellar bar in disc galaxies can appear shorter and more oval or longer and rectangular, thus influencing the bar strength measurement. The torque of the stellar bar redistributes the angular momentum within the galaxy (e.g. Lynden-Bell & Kalnajs 1972; Athanassoula 2003, 2005). This makes bars a primary and efficient driver of internal evolution through the redistribution of baryonic

★ E-mail: zoe.a.le-conte@durham.ac.uk (ZALC); dimitri.a.gadotti@durham.ac.uk (DAG)

and dark matter (e.g. Méndez-Delmestre et al. 2007; Regan et al. 2006; Di Matteo et al. 2013; Fragkoudi et al. 2018). Bar-driven gas inflow considerably impacts central galactic star formation, most notably in the formation of stellar structures, such as the nuclear disc (e.g. Sanders & Tubbs 1980; Knapen et al. 1995; Allard et al. 2006; Coelho & Gadotti 2011; de Lorenzo-Cáceres et al. 2012; Bittner et al. 2020; Gadotti et al. 2020). The bar also undergoes buckling processes forming box/peanuts (e.g. Combes & Sanders 1981; Combes et al. 1990; Ishizuki et al. 1990; Kormendy 1982; Kormendy & Kennicutt 2004; Carles et al. 2016). It is currently disputed as to whether the presence of a bar could influence the fuelling mechanisms of the active galactic nucleus (AGN) although a consensus is emerging in that bars help building a fuel reservoir near the galactic centre (e.g. Knapen et al. 1995; Alonso, Coldwell & Lambas 2013; Cisternas et al. 2015; Alonso et al. 2018; Silva-Lima et al. 2022; Garland et al. 2023). Sheth et al. (2005) confirm the result of Sakamoto et al. (1999), namely that the central kiloparsec of barred galaxies contains a higher degree of molecular gas concentrations, however in simulations Fragkoudi, Athanassoula & Bosma (2016) observe a consequential reduction in the gas inflow to the central kiloparsec due to the boxy/peanut bulge associated with the bar.

Multiple observational investigations into the abundance of stellar bars in disc galaxies up to $z \simeq 1$ find a linear decrease in their frequency with increasing redshift. A constant bar fraction within the redshift range $0.25 < z < 1.0$ in the Galaxy Evolution from Morphologies and SEDs (GEMS) survey was found in Jogee et al. (2004) where three independent techniques were used to identify spiral galaxies and ellipse fits were used to characterize barred galaxies. Abraham et al. (1999) found a decline in the bar fraction within the redshift range $0.0 < z < 1.5$ from quantitatively estimated bar strengths of galaxies in the Hubble Deep Field-North and -South. Sheth et al. (2003) identified barred galaxies by ellipse fitting techniques for galaxies within the redshift range $0.7 < z < 1.0$ in the Near-Infrared Camera and Multi-Object Spectrometer Hubble Deep Field-North. Using the 2 deg^2 Cosmic Evolution Survey (COSMOS), Sheth et al. (2008) found a decrease in the bar fraction using cross-checked visual and ellipse fitting bar identification techniques within the redshift range $0.20 < z < 0.84$. A decrease by a factor of two from $z \sim 0.4$ to ~ 1.0 in the COSMOS bar fraction was found in Melvin et al. (2014) using visual classifications. It has then been inferred from these studies that bar features cease to exist at greater lookback times, implying that bar-driven evolutionary processes do not commence until ∼6 Gyr after the big bang. These studies require high-resolution and sensitive imaging across a large sky area, which the *Hubble Space Telescope* (*HST*) has achieved. At $z \simeq 1.5$, Simmons et al. (2014) discover prominent bars in massive disc galaxies and suggest that at $\sim z > 1$, the bar fraction is sustained at $\sim$ 10 per cent. Two observational studies of the evolution of the bar fraction with redshift find no sign of a sharp decline at $z > 0.7$: Elmegreen, Elmegreen & Hirst (2004) find a near constant bar fraction of 0.23 ± 0.03 at redshifts from $z = 0$ up to $\simeq 1.1$ for a sample of 186 disc galaxies; Jogee et al. (2004) find the optical bar fraction of $\sim 0.3 \pm 0.06$ to remain at redshifts $0.2 < z < 1.0$.

In cosmological simulations, Kraljic, Bournaud & Martig (2012) found a depletion in the number of bars in present-day spiral progenitors at $0 < z < 2$, implying a violent phase of galaxy evolution where discs are dynamically hot, and there are excessive merger events. However, Athanassoula et al. (2016) follow the merging of two disc galaxies and found that the merger remnant starts forming a bar before the disc is fully developed. Rosas-Guevara et al. (2022) use TNG50 simulations (Nelson et al. 2019) to trace the bar fraction evolution with redshift and show the bar fraction to increase to ∼50 per cent at $z \simeq 1$ and only significantly decrease at $\sim z > 2$. Even at $z \simeq 6$, the simulated bar fraction, at a minimum, reaches ∼ 25 per cent. The bar fraction found in the Auriga cosmological zoom-in simulations from Fragkoudi et al. (2020) are in good agreement with observational studies, where for redshifts $0 \leq z \leq 1.5$ the bar fraction decreases from ∼70 per cent to ∼20 per cent.

Various bar identification techniques can be applied to images, including classifications by eye (e.g. Athanassoula et al. 1990; Cheung et al. 2013; Simmons et al. 2014; Buta et al. 2015). Stellar bar characterization and analysis identified structural features by eye from the colour composite images of galaxies, where participants vote a galaxy as *barred, candidate bar* or *unbarred* (e.g. de Vaucouleurs et al. 1991; Eskridge et al. 2000; Nair & Abraham 2010; Buta et al. 2015). Characteristic signatures in the radial profiles of barred galaxies can be seen, which can be used to aid or replace visual classification methods. Position angle (PA) and ellipticity (e) measurements are obtained from isophotal ellipse fits (see Section 3.1 for an explanation), in which the parameter radial profiles are used to identify a bar feature. The criteria for bar identification differ between studies but generally agree that within the bar-dominated region, the PA remains constant, and e gradually rises. The end of the bar can be defined by taking the radius of either the peak ellipticity, or the one with the minimum ellipticity succeeding the peak ellipticity, or where a significant change in PA occurs, or a combination of these three metrics (e.g. Wozniak et al. 1995; Buta et al. 1998; Elmegreen et al. 2004; Jogee et al. 2004; Marinova & Jogee 2007; Guo et al. 2023). In a volume-limited $z \leq 0.01$ Sloan Digital Sky Survey (SDSS)/DR7 sample with galaxies $M_r \leq -15.2$, Lee, Ann & Park (2019) found the bar fractions for three different identification techniques: 63 per cent by visual inspection; 48 per cent by ellipse fitting; and 36 per cent by Fourier analysis. Additionally, in their study, they concluded that ellipse fitting techniques could miss ∼ 15 per cent of visually classified bars due to large bulges in early-type spirals. Using a deep convolutional neural network, Abraham et al. (2018) identified bars in SDSS with good accuracy. Surveys are now on remarkably large scales, so automated techniques such as machine learning (e.g. Cheng et al. 2021) will become vital for morphological classifications.

The *JWST* has provided the opportunity to expand the investigation of the bar fraction to higher redshifts. Imaging from the Near Infrared Camera (NIRCam) probes the rest-frame near-infrared (NIR) emission of galaxies at redshifts up to 3 and probes the rest-frame optical at redshifts up to 7; NIR emission traces the older stellar populations which dominate bar features and are also less affected by dust extinction and recent star formation (e.g. Frogel, Quillen & Pogge 1996; Schneider 2006). In fact, the NIR bar fraction at $z \simeq 0$ is higher than the optical bar fraction (e.g. Marinova & Jogee 2007), and Buta et al. (2015) argue that this is due to stellar structural features being more perceptible. Thus, weaker bars in the optical become stronger in the NIR, so a higher bar fraction is observed. In addition, the primary mirror on *JWST* is over 2.5 times the diameter size of the *HST* primary mirror, meaning that the sensitivity of *JWST* is significantly better. The improved sensitivity, along with the longer rest-frame wavelengths probed by *JWST*, means elongated bar structures become more discernible than in their counterpart *HST* images (e.g. Huertas-Company et al. 2023). For this reason, we can now study the bar-driven evolution of galaxies with the *JWST* by searching for the epoch when stellar barred structures form in disc galaxies.

By conducting visual classifications on NIRCam *F200W* filter images of the SMACS0723 cluster at $z = 0.39$, Méndez-Abreu, Costantin & Kruk (2023) find that the bar fraction distribution is

strongly dependent on stellar mass. A previous study of stellar bars at $\sim z > 1$ using the Cosmic Evolution Early Release Science Survey (CEERS) was conducted by Guo et al. (2023) who identified six strongly barred galaxies at $z \sim 1$–3, with the highest redshift galaxy at $z \sim 2.3$. In this study, we use the initial four NIRCam *JWST* observations from CEERS to find the evolution of the bar fraction at redshifts between $z = 1$–3. To this aim, we visually classify a mass-complete sample of these high-resolution rest-frame NIR images for barred features in disc galaxies.

This paper is outlined as follows: in Section 2, we explain the NIRCam image reduction pipeline and our sample selection. Stellar bar identification techniques and our methodology for visual classifications are discussed in Section 3. In Section 4, we present the bar fraction for two redshift bins, $z = 1$–2 and 2–3, Section 5 discusses the implications of our findings on when bar-driven evolution commences and, summarize our results in Section 6. Throughout this study, we assume the latest Planck flat lambda-cold dark matter cosmology with $H_0 = 67.36$, $\Omega_m = 0.3153$, and $\Omega_\Lambda = 0.6847$ (Planck Collaboration VI 2020).

2 THE PARENT SAMPLE

To define our sample, we use the initial four public NIRCam *JWST* observations from the CEERS (PI: Filkelstein, ID = 1345, Finkelstein et al. 2023, CEERS1, CEERS2, CEERS3, and CEERS6) taken in 2022 June that overlap with the Cosmic Assembly Near-IR Deep Extragalactic Legacy Survey (CANDELS; Grogin et al. 2011; Koekemoer et al. 2011) on the Extended Groth Strip field (EGS), as well as the initial public observations for the Public Release Imaging for Extragalactic Research (PRIMER; PI: Dunlop, ID = 1837, Dunlop et al. 2021), that overlap with the CANDELS Ultra Deep Survey (UDS) Field observations. Together, the data covers ~ 30 arcmin^2 of an area with CANDELS *HST* overlap.

2.1 Data reduction pipeline

We reprocess all of the uncalibrated lower-level *JWST* data products following a modified version of the *JWST* official pipeline. This is similar to the process used in Adams et al. (2023) and exactly the same reductions as used in Ferreira et al. (2023), which can be summarized as follows: (1) we use version 1.6.2 of the pipeline with the Calibration Reference Data System (CRDS) version 0942 which was the most up-to-date version at the time these data products were generated. Use of CRDS 0942 is essential for zero-point issues as discussed in Adams et al. (2023). (2) We apply the 1/*f* noise correction derived by Chris Willott on the resulting level 2 data of the *JWST* pipeline.[1] (3) We extract the sky subtraction step from stage 3 of the pipeline and run it independently on each NIRCam frame, allowing for quicker assessment of the background subtraction performance and fine-tuning. (4) We align calibrated imaging for each individual exposure to *Gaia* using TWEAKREG, part of the DRIZZLEPAC Python package.[2] (5) We pixel match the final mosaics with the use of ASTROPY REPROJECT. The final resolution of the drizzled images is 0.03 arcsec pixel^{-1}.

Furthermore, an additional step was added for the PRIMER reductions in step (2) above due to the presence of a significant stripping pattern artefact at a 45° angle in the NIRCam footprint, resembling the diffraction pattern of a bright star outside the field of view of the camera. This issue was removed with an adaptation of the 1/*f* noise algorithm, first rotating the observations to 45° to align the pattern with one of the axes, followed by a background subtraction for each row based on the background mean of that row. Finally, the adjusted file is rotated back to its original orientation. This drastically reduces the artefact in the final products, although some are still visible in colour composites due to the non-uniform nature of the artefact across different NIRCam filters. Galaxy stamps that present these residual artefacts are flagged during subsequent classification as described in Section 3.3.

Each one of the four June CEERS observations was processed into individual mosaics, while the PRIMER UDS observations were stacked in a single mosaic due to the large overlapping area.

2.2 Sample selection

As a way to produce a selection with robust photometric redshifts and stellar masses, we use the CANDELS-based catalogues produced by Duncan et al. (2019) that include observations from *HST*, *Spitzer*, and ground-based facilities. These redshifts are robustly calibrated from spectroscopic redshifts, with an average outlier fraction of $\frac{|\Delta z|}{1+z_{\rm spec}} \sim 5$ per cent (see Duncan et al. 2019 for details).

From these catalogues, we select all sources that lie within the footprint of the CEERS and PRIMER observations outlined previously. All sources with photometric redshifts and stellar masses that are present in both CANDELS and the new *JWST* observations are selected. Additionally, no magnitude or signal-to-noise cut is done to mitigate any selection bias due to different sensitivities between *HST* and *JWST*, which prevents *JWST* bright galaxies from being excluded if they are faint in *HST* bands. Then, all overlapping sources between $1 \leq z \leq 3$ are selected, resulting in a parent sample of 5218 galaxies present within the combined area of CEERS + PRIMER and 5445 galaxies in the area of CANDELS EGS and UDS fields, including 3559 galaxies with visual *Hubble*-type classifications from Ferreira et al. (2023) at $z > 1.5$. We note that some galaxies fall in the gaps between the NIRCam detectors, and therefore, while they are included in the *HST* sample, they cannot be analysed with *JWST* data.

For each of the CEERS + PRIMER 5218 galaxies in the sample, we produce 30 mas 128×128 pixel cutouts for the *JWST* filters, namely *F356W* and *F444W*. Concerning the 5445 CANDELS galaxies observed with the *HST* Wide Field Camera 3 (WFC3) filters, namely *F160W*, we produce 60 mas 64×64 pixel cutouts covering a consistent angular field of view, enabling us to probe the same galaxies in a relatively similar wavelength regime between the two instruments. In this study, we select the *F444W JWST* filter and compare these galaxies to their *HST* WFC3 filter *F160W*.

3 BAR IDENTIFICATION

The random orientation of galaxies challenges observational attempts of bar measurements. Stellar bars are distinguishable in near-face-on galaxies and become less well defined in high-inclination galaxies. This study aims to determine the fraction of disc galaxies that harbour a bar in an optimized sample of *F444W* NIRCam and *F160W* WFC3 images. For our bar identification process, we use visual inspection of galaxy images as well as radial profiles of PAs and ellipticity.

3.1 Sample optimization

Considering the challenges involved in the identification of bars, as noted above, we choose to remove highly inclined and overly

[1] https://github.com/chriswillott/jwst
[2] https://github.com/spacetelescope/drizzlepac

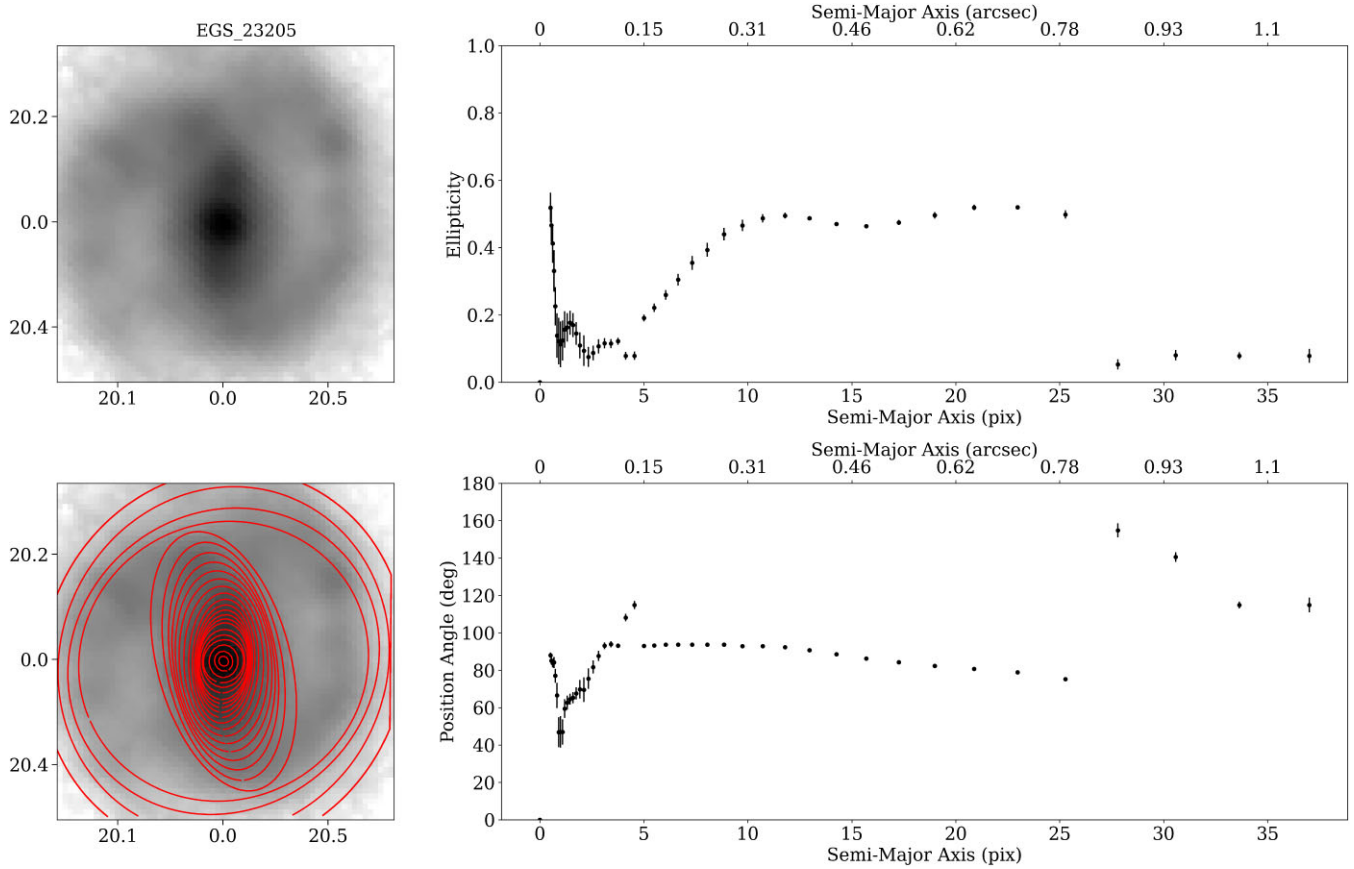

Figure 1. Elliptical isophotal fits using the module PHOTUTILS.ISOPHOTE from Python'sASTROPY package (Bradley et al. 2022) to logarithmic *F444W* NIRCam images of the galaxy EGS_23205 at redshift $z \sim 2.12$. The left-hand side shows the *F444W* image annotated with the pixel coordinates (top) and superposed elliptical isophotal fits (bottom). The right-hand side shows radial profiles of the ellipticity (e) (top) and PA in degrees (bottom) as derived from the ellipse fits.

faint or poorly resolved galaxies from the sample through an automated process. This optimization process is intended to remove only galaxies that would be visually classified as ambiguous or unclassifiable. To do so, we fit ellipses to the isophotal contours of all galaxies in the parent sample to extract radial profiles of e and PA (see e.g. Gadotti et al. 2007; Barazza, Jogee & Marinova 2008; Barazza et al. 2009; Aguerri et al. 2009). Fig. 1 shows in the left panel the ellipse fits superposed on the *F444W* NIRCam image of the galaxy EGS_23205, and in the right panel, radial profiles of the e and PA of the fitted ellipses. EGS_23205 is an example of a barred galaxy in this study and is observed relatively face-on.

Before visually classifying galaxies as barred or unbarred, we apply a three-step procedure to obtain our final, optimized galaxy sample containing galaxies in which a bar can be identified robustly: (1) ellipse-fitting to NIRCam images without fixing the centre; (2) second ellipse-fitting with fixed centres; and (3) removal of highly inclined galaxies. In the following, we give a detailed explanation of these three steps:

Phase 1. Elliptical isophotes are fitted to *F444W* NIRCam images of the *JWST* galaxy sample and analysed using PHOTUTILS.ISOPHOTE from Python's ASTROPY package (Bradley et al. 2022). This package uses an iterative method to measure the isophotes (Jedrzejewski 1987). The objective at this optimization phase is to eliminate the overly disturbed or extremely poorly resolved or low surface brightness galaxies that are visually unclassifiable. In general, the algorithm fails to produce any result when applied to these objects. Therefore, at this stage, all galaxies for which fits can be obtained successfully are kept, even if the fits do not perfectly align with the galaxy. Approximately 30 per cent of the parent sample had successful ellipse fits in the *F444W* filter. The remaining $\sim$ 70 per cent of galaxies that failed ellipse fittings are overly disturbed, poorly resolved, and/or low surface brightness systems and removed from the sample. In addition, in a small number of cases, these were images of point sources conspicuously showing the *JWST* point spread function (PSF), in which secondary PSF features prevent a successful fit.

Phase 2. The ellipses fitted in the previous step do not have a specified centre, which may prevent the correct identification of highly inclined galaxies. We thus take the inner 40 per cent of the isophotes fitted to the galaxy in the first step, exclude the inner 10 per cent isophotes and take the average position of the centre of these isophotes as the galaxy centre. The choice for this range of radii ensures that one has enough pixels to compute a statistically robust position of the galaxy centre and simultaneously avoids strongly asymmetric structures, which are often at larger radii. By using isophotes all the way to 40 per cent of the fitted outer radius, we minimize the impact that a bright close-to-central point source would have in shifting the centre of isophotal fits from the correct galaxy centre. Visually inspecting the fits, we see that this is not a significant issue. It is also important to note that a bright point source overlapping with the galaxy will often result in the galaxy being visually unclassifiable, removing it from the sample at Phase 1. In addition, a function assesses the pixel values in a 10×10 pixels window centred at the new galaxy central pixel coordinates to

ensure that bright foreground stars do not influence the determination of the galactic centre. To improve convergence stability against non-elliptical structures, including stars, PHOTUTILS.ISOPHOTE clears aberrant points from each isophote with a *k*-sigma algorithm. We then re-run PHOTUTILS.ISOPHOTE on *F444W* NIRCam galaxy images with fixed specified central positions. With fixed centres, the ellipse fits failed for approximately 26 per cent of the newly optimized sample. We verified that the failed ellipse fits correspond to galaxies with overly irregular or ambiguous morphology. These systems are also removed from the sample. We use the default scheme developed in Jedrzejewski (1987) to decide when the fitting stops. By visually inspecting the fits, we verified that the fits only rarely stop before reaching the outskirts of the galaxy.

Phase 3. An inclination limit of $i \leq 60^{\circ}$ is applied to remove highly inclined galaxies as it is difficult to identify if a bar is present in these cases. We define the inclination of a galaxy by measuring the ellipticity of the outermost fitted ellipse,

$$e = 1 - \frac{b}{a}, \tag{1}$$

where b is the minor axis length and a is the major axis length. The inclination is defined as

$$\cos i = \frac{b}{a}. \tag{2}$$

Approximately 34 per cent of the galaxies in the *F444W* filter of the newly optimized sample were seen to be too highly inclined and were removed from the sample. While highly inclined, disturbed and edge-on galaxies have been removed in this and the previous phases of the optimization, we note that a residual fraction of regular disc galaxies with inclination larger than 60° still went through to the optimized sample despite this final optimization step. Conservatively, we treated these galaxies as all remaining ones, which means our final bar fractions could be slightly underestimated (although, in some cases, a bar could be seen despite the high inclination). We speculate that a combination of the relatively poor physical spatial resolution and lower outer surface brightness compared to local galaxies is the cause behind these residual highly inclined galaxies remaining in the optimized sample.

We applied this three-step optimization procedure to our initial large CEERS *F444W* galaxy sample, ensuring elliptical isophotes could be fitted to the galaxy image with an identified galactic centre and that the galaxy was not edge-on. The resultant optimized sample of galaxies suitable to our analysis is 768 CEERS images in the NIRCam *F444W* filter (hereafter referred to as the optimized *JWST* sample). Of the optimized galaxy sample, 404 galaxies are between the redshifts $1 \leq z \leq 2$, and 364 galaxies are between the redshifts $2 < z \leq 3$. Before visual classifications, a co-author (DG) visually verified that all removed objects were indeed poorly resolved, overly faint/irregular, or too inclined. Table 1 gives the number of galaxies removed at each phase and the resultant galaxy sample size.

To measure the difference in the bar fraction between *JWST* and *HST*, we also applied the three-step optimization procedure in our *HST* CANDELS *F160W* galaxy sample. This reduced our *HST* CANDELS sample to an optimized sample of 133 galaxies (hereafter referred to as the optimized *HST* sample). The reduced sensitivity and bluer wavelength range of *HST* means many of the galaxies are very pixelated, and features are difficult to discern. Therefore, the ellipse fitting technique failed on many of these galaxies, greatly reducing the optimized *HST* sample size.

Table 1. Number of galaxies removed from the sample and the resultant sample size after each optimization phase.

Phase	*HST*		*JWST*	
	$N_{\rm gal}$ removed	$N_{\rm gal}$ remain	$N_{\rm gal}$ removed	$N_{\rm gal}$ remain
1	4980	465	3635	1583
2	230	235	416	1167
3	102	133	399	768

Notes. Column (1): the optimization phase. Columns (2) and (3) are in the context of *HST* CANDELS *F160W* images. Column (2): the number of galaxies which failed to meet the phase criteria. Column (3): the sample size after the criteria are applied, with phase 1 being applied to the parent sample. Columns (4) and (5) are the same as columns 2 and 3, but in the context of *JWST* CEERS *F444W* images.

3.2 Disc identification

Naturally, the bar fraction is the number of barred galaxies divided by the number of disc galaxies, and we therefore need first to compute the latter. The variations in morphological appearance and dependence on orientation make disc galaxies challenging to identify visually. Given the different wavelength ranges probed by *JWST* and *HST*, we compute the disc fraction in our parent samples to avoid any potential bias from our optimization procedure in the number of disc galaxies and extrapolate that to the optimized sample. This is also important as the optimized sample is significantly smaller than the parent sample, and uncertainties thus become more significant. We obtain the *JWST* disc fraction from the published visual classifications by co-author LF and collaborators (Ferreira et al. 2023). Six independent participants visually classified 3559 CEERS sources in their rest-frame NIR images, using the NIRCam filters *F277W*, *F356W*, and *F444W* for the redshifts $z = 1.5$–3.0, which contained 1531 discs. The disc fraction found by LF does not extend to the lower end of the redshift range selected for this study, however we assume that the disc fraction between redshifts 1 and 1.5 is the same as between redshifts 1.5 and 2. For the redshift bins $1 \leq z \leq 2$ and $2 < z \leq 3$, the disc fraction of the optimized *JWST* sample is thus $f_{\rm disc} = 0.49 \pm 0.039$ and 0.39 ± 0.046, respectively. The systematic error on $f_{\rm disc}$ is the standard error of $f_{\rm disc}$ found by the six participants in Ferreira et al. (2023). By extrapolating $f_{\rm disc}$ to the optimized *JWST* sample, the number of disc galaxies $count_{disc} = 196$ and 143 for $1 \leq z \leq 2$ and $2 < z \leq 3$, respectively.

For the *HST* sample, we use the visual classifications by Kartaltepe et al. (2015) to determine the optimized *HST* $f_{\rm disc}$. For the redshift bins $1 \leq z \leq 2$ and $2 < z \leq 3$, the disc fraction of the *HST* parent sample is $f_{\rm disc} = 0.75$ and 0.78, respectively. It is important to point out that the detailed classification of Kartaltepe et al. (2015) includes disc galaxies in the category 'irregular', which is also further subdivided in categories such as 'spheroid and irregular' to separate disc galaxies that are irregular from both disc galaxies with regular morphology and spheroidal galaxies that are irregular. We thus include in $f_{\rm disc}$ a smaller fraction of galaxies ($\sim$ 15 per cent) noted as irregulars (but after removing those noted as 'spheroid and irregular') following strictly the classifications of Kartaltepe et al. It is important to include these galaxies in $f_{\rm disc}$ because these are disc galaxies despite their disturbed morphology, and their discs can develop bars. The Large Magellanic Cloud is a notable example of an irregular galaxy with a disc that hosts a bar. Furthermore, Kartaltepe et al. (2015) show that the Sérsic index and colour distributions of their galaxies classified as irregulars match the corresponding distributions of the galaxies classified as discs. And, indeed, some of the barred galaxies we find were classified as irregulars in Kartaltepe et al. (2015, see our

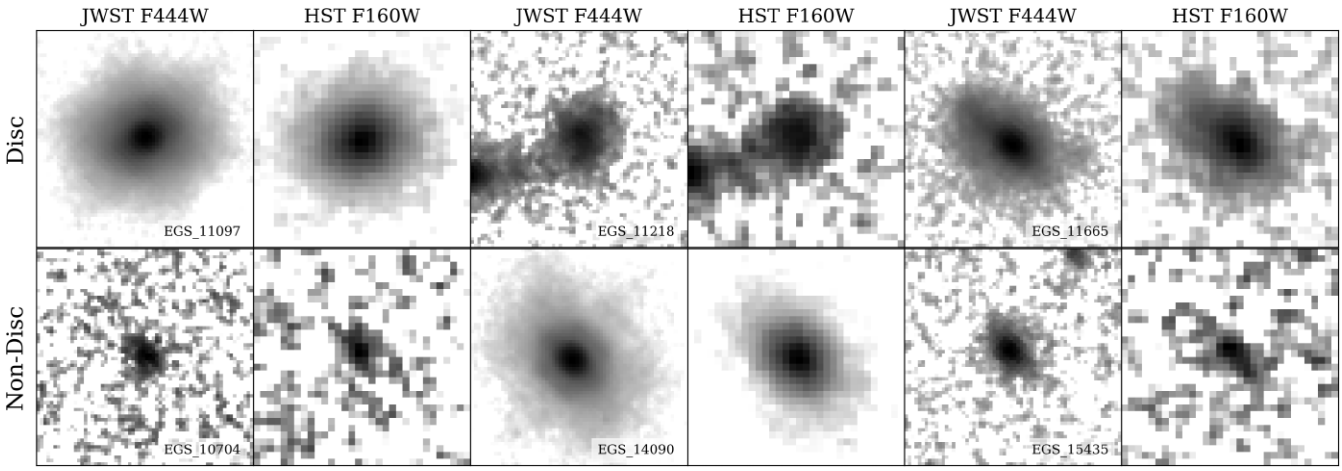

Figure 2. Rest-frame NIR logarithmic images of three disc (top row) and three non-disc (bottom row) galaxies. The three exemplars for each classification, with IDs in the lower right of the NIRCam *F444W* image, are shown in the *JWST* NIRCam *F444W* (left) and *HST* WFC3 *F160W* (right).

Table A1). The systematic error on $f_{\rm disc}$ is the standard error of $f_{\rm disc} = \pm 0.026$ found by comparing the results from the three classifiers in Kartaltepe et al. (2015). By extrapolating $f_{\rm disc}$ to the optimized *HST* sample, $\rm count_{disc} = 81$ and 19 for $1 \leq z \leq 2$ and $2 < z \leq 3$, respectively. We note that the *HST* disc fraction may be a lower limit since Nelson et al. (2023), using *JWST*, found that massive, dusty edge-on discs could have been missed as *HST*-dark galaxies. This would induce an overestimation of the bar fraction with *HST* data.

Additionally, two co-authors (ZLC and DG) also visually classified the optimized *JWST* sample to study the stellar mass distributions of barred and unbarred galaxies in the optimized sample, discussed further below. The participants voted the galaxy to be a disc or non-disc based on the *F444W* NIRCam images and a log intensity radial profile. In principle, artefacts (discussed in Section 2.1) could mislead visual classifications, but these PSF effects are clearly distinguishable. The diffraction spikes mostly appeared as a large hexagon over the galaxy image, so the galaxy is not elongated in one direction preferentially. Therefore, we typically class these as non-discs/unidentifiable. To ensure we were not affected by less prominent artefacts, we checked for effects in the intensity radial profile of each galaxy. Fig. 2 shows three examples of disc and three non-disc galaxies in rest-frame *JWST* NIRCam *F444W* and *HST* WFC3 *F160W* filters. Non-disc galaxies can include strong PSF-affected sources, as shown by the central source in the figure. In this classification, the average disc fraction of the optimized *JWST* sample is $f_{\rm disc} = 0.40 \pm 0.14$ for the full redshift range $1 \leq z \leq 3$ (the quoted uncertainty is the difference in $f_{\rm disc}$ found by the two participants). The disc fraction derived in this study thus agrees with the disc fraction found by LF and collaborators (Ferreira et al. 2023), which corresponds to 0.45 ± 0.034 when we employ their classifications and consider our optimized sample at $1.5 \leq z \leq 3$.

3.3 Bar visual classifications

The optimized *JWST* sample was then visually classified by five co-authors (ZLC, DG, CdSF, TK, and JN). The participants were asked to vote *barred, maybe-barred* or *unbarred* on the *F444W* NIRCam images. The votes were tallied, and a galaxy was classified as follows: a galaxy is classified as strongly barred if it obtained at least three out of five votes for barred; a galaxy is classified as weakly barred if it obtained two out of five votes for barred or at least three out of five votes for maybe-barred; a galaxy is classified as unbarred if it did not obtain the vote thresholds. Fig. 3 is a histogram of the number of barred and maybe-barred votes the co-authors gave on each galaxy in the optimized *JWST* sample. The figure does not show the galaxies where the co-authors were congruent about the galaxies being unbarred. The figure shows the difficulties in identifying bars as 75 per cent of the galaxies shown here are below the vote threshold, hence classified as unbarred.

The visual classification method was then repeated for the optimized *JWST* sample in the NIRCam *F356W* filter. The resolution marginally improves at this shorter wavelength, so structural features are better defined. However, this wavelength can be more subjected to dust extinction and star formation effects, so the bar-dominated evolved stellar populations may be only moderately traced. The overall bar fraction did not change between the two NIRCam filters, but a few weaker bars became stronger when observed in the filter *F356W*. Finally, the visual classification method was repeated again on the optimized *HST* sample. EGS_31125 is shown in Fig. 4 in the three different filters employed: *HST* WFC3 *F160W* and *JWST* NIRCam *F356W* and *F444W*. EGS_31125 is classified in the *F444W* filter as strongly barred and unbarred in the *F160W* filter. This figure clearly shows the impact of improved sensitivity and longer wavelength with *JWST* on the galaxy at redshift $z \simeq 2.06$ and how distinctive the disc structures become (see also Guo et al. 2023). On the other hand, it is interesting to note that 15 galaxies have been classified as barred in the *HST* sample but did not receive any vote when classified using the *JWST* data. These images were inspected again, and while these galaxies could indeed be barred, we note that in some cases, effects from the *JWST* PSF impact the classification. In other instances, details in the structure of the galaxy are better discerned in the *JWST* images, rendering the impression of a bar somewhat uncertain. We show examples of these galaxies in Fig. B1 (Appendix B).

4 THE BAR FRACTION

We aim to determine the fraction of the disc galaxy population at redshifts $z = 1$–3 hosting a bar. We visually classified the optimized *JWST* sample, which met the criteria described in Section 3.1. The process is repeated for the optimized *HST* sample to explore if an increase in the bar fraction is found using *JWST*. Galaxies were classified as described in Section 3.3. Fig. 5 shows three examples of strongly barred, weakly barred and unbarred galaxies in the *JWST*

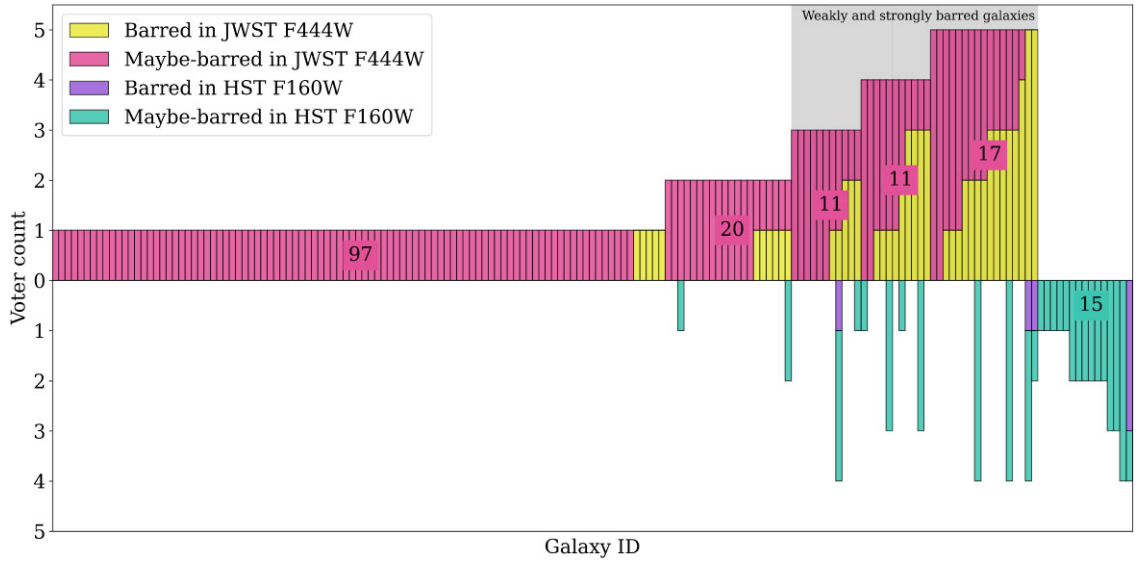

Figure 3. Distribution of the total number of barred in yellow (purple) and maybe-barred in pink (green) votes cast by the five participating co-authors to candidate galaxies in the optimized *JWST* (*HST*) sample in the upper (lower) panel. 171 galaxies received barred or maybe-barred votes in the NIRCam *F444W* filter or WFC3 *F160W* filter from the classifiers, and 597 galaxies received zero votes. The number of galaxies in each voter count category is shown. A grey-shaded area covers the galaxies which are classified as weakly or strongly barred. We exclude galaxies that received zero-barred or maybe-barred votes from this figure.

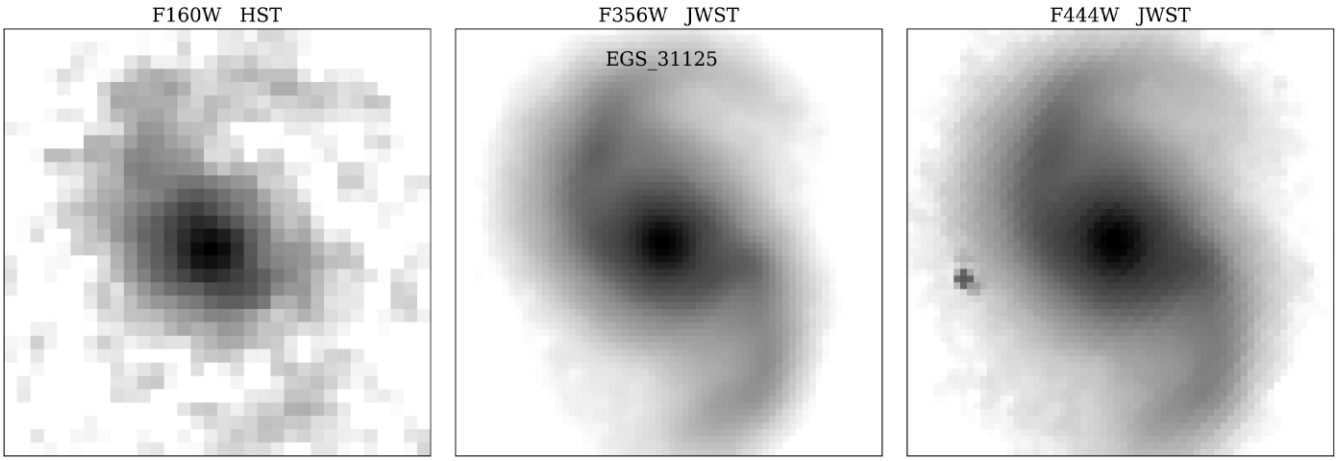

Figure 4. The logarithmic image of galaxy EGS_31125 at redshift $z \simeq 2.06$, visually classified as strongly barred from the *JWST* NIRCam *F444W* image, shown in an *HST* filter and two *JWST* filters. From left to right: *HST* WFC3 *F160W* and *JWST* NIRCam *F356W* and *F444W*. This filter comparison demonstrates the effects of PSF, sensitivity, and wavelength range on a galaxy image, particularly in the context of bars. The image shows EGS_31125 in rest frame 0.52, 1.16, and 1.45 μm, respectively.

NIRCam *F444W* and *HST* WFC3 *F160W* filters. The strongly barred galaxies have distinct stellar structures, while some weakly barred galaxies have less prominent outer discs.

The bar fraction is found for two redshift bins, $1 \leq z \leq 2$ and $2 < z \leq 3$, to observe the evolution of the bar fraction. The redshift was only divided into two bins, as the number of barred galaxies is relatively small. In the optimized *JWST* sample, 29 galaxies were identified as barred in the lower redshift bin, where eight are strongly barred, and 21 are weakly barred, which decreased to ten barred galaxies in the higher redshift bin, where five are strongly barred, and five are weakly barred. All galaxies classified as barred are shown in Appendix A: Fig. A1 shows the strongly barred galaxies, while Fig. A2 shows the weakly barred galaxies. The 39 barred galaxies are listed in Table A1, along with their photometric redshift and *HST* visual classifications from Kartaltepe et al. (2015) of which only one galaxy was identified as barred. In the optimized *HST* sample, nine galaxies were identified as weakly or strongly barred in the lower redshift bin, and only one weakly barred galaxy was identified in the higher redshift bin.

It is debated how the bar fraction depends on the stellar mass (e.g. Barazza et al. 2008; Sheth et al. 2008; Nair & Abraham 2010; Masters et al. 2011; Melvin et al. 2014; Gavazzi et al. 2015; Erwin 2018). In Fig. 6, we show the stellar mass distribution as a function of redshift for all disc galaxies in the optimized sample. The disc galaxies are taken from the classification of one of the participants in the disc classification procedure (ZLC). Still, we verified that qualitatively similar results are found regardless of the classifier. The 95 per cent empirical completeness limit of the sample, as estimated in Duncan et al. (2019), is indicated, showing that most of our sample is above

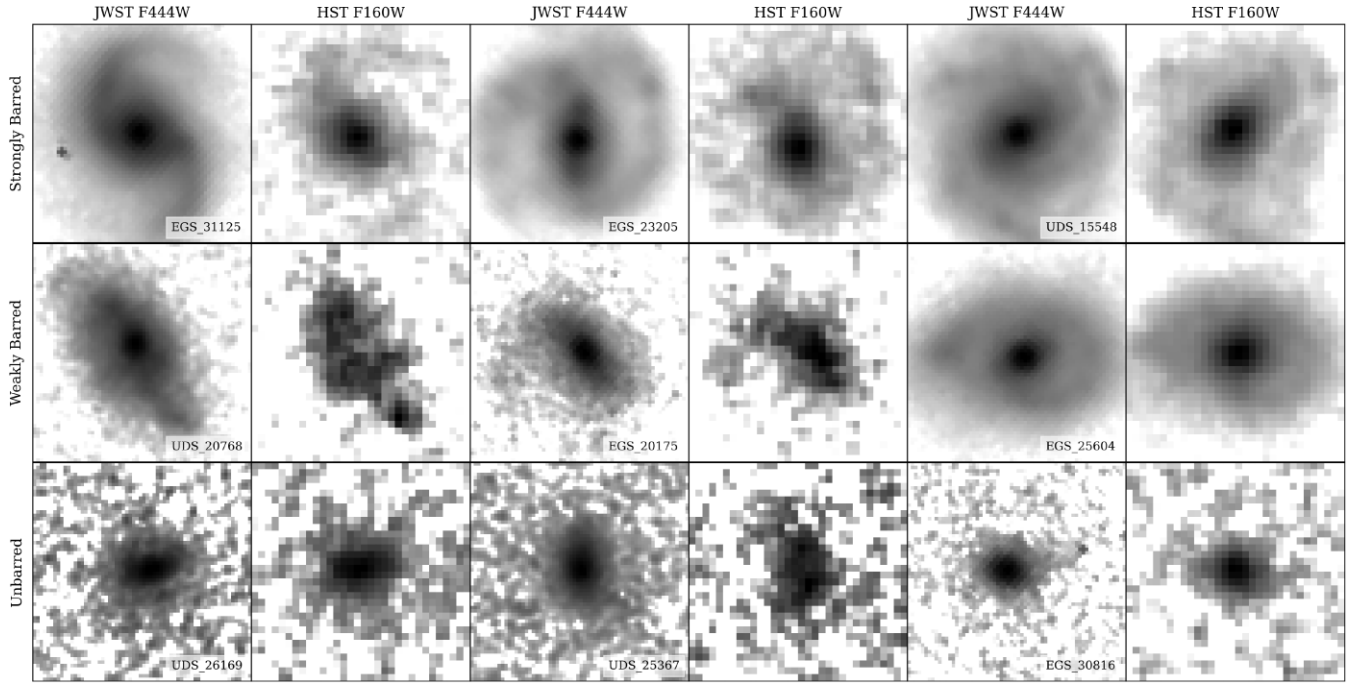

Figure 5. Rest-frame NIR logarithmic images of three strongly barred (top row), weakly barred (middle row), and unbarred (bottom row) galaxies. The three exemplars for each classification, with IDs in the lower right of the NIRCam *F444W* image, are shown in the *JWST* NIRCam *F444W* (left) and *HST* WFC3 *F160W* (right).

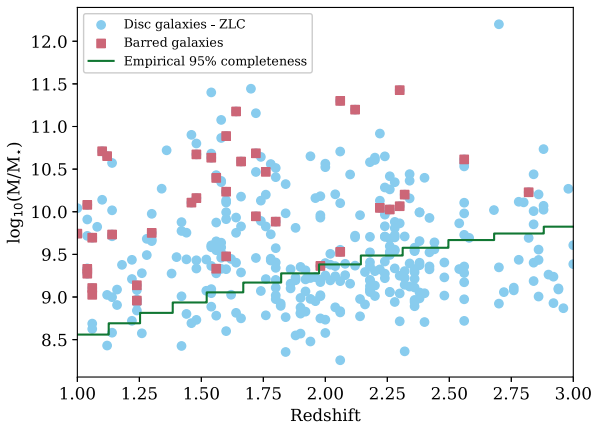

Figure 6. Distribution of stellar masses for the sample of disc galaxies as classified by ZLC in *JWST* CEERS between the redshifts $1 \leq z \leq 3$. Disc galaxies are shown as circles, while the weakly and strongly barred galaxies are squares. A stepwise line shows the 95 per cent empirical completeness of the sample (see fig. 8 of Duncan et al. 2019). The parameter space below this line in this plot corresponds to a completeness fraction of $\approx 85 - 90$ per cent.

or close to the completeness limit. Interestingly, this figure shows that barred galaxies tend to avoid the least massive galaxies at each redshift, in line with the results from Sheth et al. (2008). In order to calculate the bar fraction in a sample as complete in mass as possible, we apply the 95 per cent completeness step function as a mass limit, that is, we select galaxies above the 95 per cent completeness line. This includes a new computation of the disc fractions as above but now only for galaxies above the 95 per cent completeness line, which slightly increases the disc fractions for both *HST* and *JWST*. For the redshift ranges $1 \leq z \leq 2$ and $2 < z \leq 3$, the *JWST* bar fraction is $\approx 17.8^{+5.1}_{-4.8}$ per cent and $\approx 13.8^{+6.5}_{-5.8}$ per cent, and the *HST* bar fraction is $\approx 11.2^{+4.7}_{-3.8}$ per cent and $\approx 6.0^{+8.4}_{-3.7}$ per cent, respectively. The uncertainties on these bar fractions are the sum in quadrature of the systematic and statistical errors, which are discussed below. For a 95 per cent complete stellar mass sample, the fraction of bars found in disc galaxies in *JWST* is approximately twice that in *HST*. Table 2 shows the progression of the *JWST* and *HST* galaxy sample sizes after the different selection and classification criteria are applied.

Fig. 7 shows the visually classified bar fraction versus redshift and lookback time in the context of other observational work assessing bar fractions using *HST*. The figure shows that previous results based on *HST* data indicate a decline in the bar fraction from lower to higher redshifts. While the *JWST* bar fraction also decreases from the redshift bin $1 \leq z \leq 2$ to the redshift bin $2 < z \leq 3$, the *JWST* bar fraction in the lower redshift bin is greater than the *HST* bar fraction in the same redshift bin. A dashed line indicates the redshift range of our visually identified barred galaxies, and a thick solid line indicates the distribution quartiles, that is, 25 per cent-75 per cent. We identify the highest redshift strongly barred galaxy as EGS_24268 at $z \simeq 2.32$ (also found in Guo et al. 2023) and the highest redshift weakly barred galaxy as EGS_22729 at $z \simeq 2.82$.

The Jeffreys interval (Brown, Cai & DasGupta 2001; Gelman et al. 2003) is used to determine the statistical uncertainty in the computed bar fractions. Considering the fraction of a large population with a given attribute (i.e. bars) and neither close to 0 nor 1, the normal approximation can be assumed to derive uncertainties, but for small sample sizes and extreme population proportion values (e.g. the *HST* bar fraction at $2 < z \leq 3$), Cameron (2011) convincingly argues for a beta distribution quantile technique over the 'normal approximation' and the Clopper & Pearson (1934) approach, in which the Jeffreys 'non-informative' prior can be used interchangeably with the uniform prior. We adopt this method to estimate the full 68 per cent confidence intervals of the bar fraction in the two redshift bins. The sample

Table 2. Progression of the galaxy sample sizes after the different selection and classification criteria are applied.

Sample	Redshift	Sample sizes $N_{\rm gal,HST}$	$N_{\rm gal,JWST}$	$N_{\rm gal,HST}$ Mass complete	$N_{\rm gal,JWST}$ Mass complete	Criteria applied
Parent sample	$1 \leq z \leq 3$	5445	5218	1299	1180	Redshift
Optimized sample	$1 \leq z \leq 3$	133	768	126	368	Ellipse fitting, $i \leq 60^{\circ}$
	$1 \leq z \leq 2$	108	404	105	237	
	$2 < z \leq 3$	25	364	21	131	
Disc sample	$1 \leq z \leq 3$	100	339	98	229	*HST* discs from Kartaltepe et al. (2015) and
	$1 \leq z \leq 2$	81	196	81	157	*JWST* discs from Ferreira et al. (2023)
	$2 < z \leq 3$	19	143	17	72	
Weakly barred	$1 \leq z \leq 3$	9	26	9	25	Visually classified bars
	$1 \leq z \leq 2$	8	21	8	20	
	$2 < z \leq 3$	1	5	1	5	
Strongly barred	$1 \leq z \leq 3$	1	13	1	13	Visually classified bars
	$1 \leq z \leq 2$	1	8	1	8	
	$2 < z \leq 3$	0	5	0	5	
		The bar fraction				
Bar fraction	$1 \leq z \leq 2$	$0.11^{+0.05}_{-0.04}$	$0.15^{+0.05}_{-0.05}$	$0.11^{+0.05}_{-0.04}$	$0.18^{+0.05}_{-0.05}$	$\frac{N_{\rm weakly\_barred}+N_{\rm strongly\_barred}}{N_{\rm disc}}$
	$2 < z \leq 3$	$0.05^{+0.08}_{-0.04}$	$0.07^{+0.07}_{-0.06}$	$0.06^{+0.08}_{-0.04}$	$0.14^{+0.07}_{-0.06}$	

Notes. Column (1): the sample label. Column (2): the redshift range. Column (3): the number of galaxies after applying the criteria to *HST* CANDELS *F160W* images. Column (4): the number of galaxies after applying the criteria to *JWST* CEERS *F444W* images. Columns (5) and (6): the same as columns (3) and (4), but with the 95 per cent mass completeness cut applied to the sample from Duncan et al. (2019). Column (7): the criteria applied. The bar fractions derived before and after applying the 95 per cent mass completeness limit are given for the two redshift bins at the bottom of the table. The bar fraction errors are explained in Section 4.

used in this study is mass complete, meaning we do not account for incomplete sampling in the uncertainty estimates. On the other hand, the more important systematic errors in our analysis stem from the difficulty of defining a galaxy as a disc or barred galaxy. The fraction of disc galaxies was taken from Kartaltepe et al. (2015, *HST* disc fraction) and Ferreira et al. (2023, *JWST* disc fraction). The standard error of the mean of the disc fraction found by the participants in the two independent studies is interpreted as the main systematic error in the bar fractions. Hence, we sum in quadrature the systematic and statistical errors of the bar fractions to obtain the final uncertainties quoted above. The statistical errors for the lower and higher redshift bins are, respectively, $^{+0.041}_{-0.030}$ and $^{+0.083}_{-0.035}$ for *HST*, and $^{+0.033}_{-0.028}$ and $^{+0.046}_{-0.035}$ for *JWST*. The systematic errors for the lower and higher redshift bins are, respectively, ± 0.023 and ± 0.011 for *HST*, and ± 0.039 and ± 0.046 for *JWST*.

5 DISCUSSION

Using NIRCam *F444W* images, corresponding to NIR rest frame at $1 \leq z \leq 3$, the visually identified fraction of disc galaxies hosting a bar at redshifts $z = 1$–2 is $\sim$18 per cent, which decreases to $\sim$14 per cent at redshifts $z = 2$–3. We found the bar fraction obtained from the *F444W JWST* images to be greater than that obtained using *F160W HST* images by a factor of about two, as shown in Fig. 7. Our value of the bar fraction at $z = 1$–2, which we derive using *HST* images, is in line with the estimate from Simmons et al. (2014, see their fig. 6) who also use *HST* data for their estimates. This begs the question, why do we find more bars in *JWST* than in *HST* images? Considering that the parent sample was chosen to contain sources present in both *HST* CANDELS and *JWST* CEERS and that the same bar-detection method was applied to both the *JWST F444W* and *HST F160W* images, the considerable difference between the *JWST* and *HST* bar fractions at each redshift bin implies that the identification of bars in disc galaxies is dependent on the sensitivity and wavelength range of the instrument; the bar fraction increases at longer wavelengths and with improved sensitivity. Spatial resolution does not play a role here. Defining the resolution of an instrument as the full width at half-maximum (FWHM) of the empirical PSF the resolution of *HST* at 1.6 μm is 0.151 arcsec[3] and the resolution of *JWST* at 4.44 μm is 145 arcsec,[4] and therefore, both instrumental setups have very similar resolution.

Interestingly, the *HST* bar fractions at the two redshift bins do not change significantly after applying the 95 per cent mass completeness limit, whereas the *JWST* bar fraction at $2 < z \leq 3$ increases substantially (although within the error bars). This may reflect the ability of *JWST* to detect more low-mass discs at high redshifts than *HST*, but still not facilitate the finding of the presumably shorter bars in low-mass discs, since the spatial resolutions of the *HST* and *JWST* images used in this work are comparable.

Our results build upon the previous studies, which find that bar-driven internal evolutionary processes for settled disc populations begin at $z \simeq 1$, whereas our new results suggest this to be $z \simeq 2$ or more. Our study finds that a sizable population of barred galaxies exists at $z \leq 3$, implying that massive disc galaxies can become dynamically settled with prominent bars at a lookback time of $\sim$11 Gyr. The idea that bar-driven galaxy evolution happens in some cases at $z > 2$ is generally consistent with the early bar formation epochs estimated for local galaxies in the Time Inference with MUSE in Extragalactic Rings (TIMER) project (Gadotti et al. 2019). For NGC 4371, it has been estimated that the bar formation happened at $z \approx$

[3]psf fwhm taken from the *hsT* user documentation: https://hst-docs.stsci.edu/wfc3ihb/chapter-7-ir-imaging-with-wfc3/7-6-ir-optical-performance
[4]PSF FWHM taken from the *JWST* user documentation: https://jwst-docs.stsci.edu/jwst-near-infrared-camera/nircam-performance/nircam-point-spread-functions

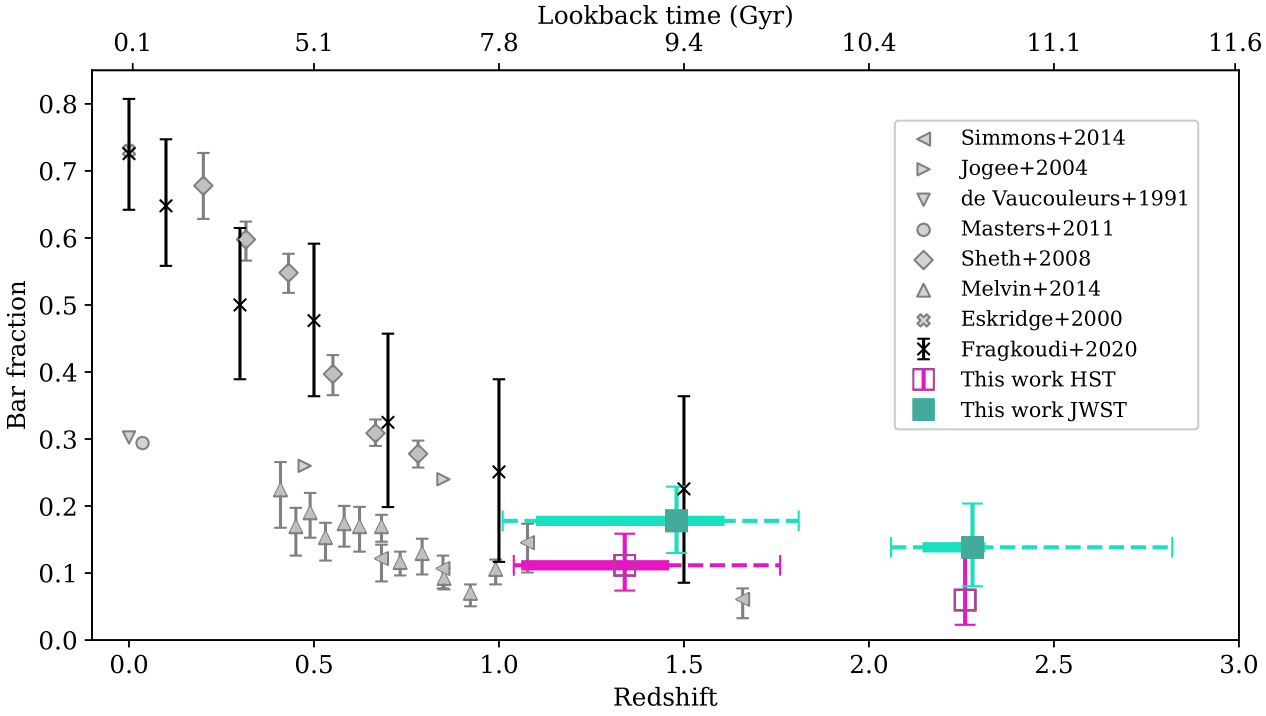

Figure 7. Evolution of the fraction of stellar bars in disc galaxies with redshift in the context of other bar assessment work using *HST*. The fractions of barred disc galaxies found in *JWST* NIRCam images are shown as filled squares, and the fractions of barred disc galaxies found in this study in *HST* WFC3 images are shown as empty squares. The bar fraction was found for two redshift bins, $1 \leq z \leq 2$ and $2 < z \leq 3$, where the marker indicates the median redshift of the barred galaxies. All of the bar fraction errors, in this study, indicate the sum in quadrature of the systematic and statistical errors. A dashed line indicates the redshift range of barred galaxies. A thick solid line indicates the redshift range of the quartiles 25 per cent–75 per cent of the barred galaxies distribution. At low redshifts, de Vaucouleurs et al. (1991, down-pointing triangle) and Masters et al. (2011, circle) found strong bars in a third of disc galaxies, while Eskridge et al. (2000, cross) found strong and weak bars in over two-thirds of disc galaxies. Simmons et al. (2014, left-pointing triangles), Sheth et al. (2008, diamonds), and Melvin et al. (2014, up-pointing triangles) found a decreasing trend of the bar fraction for higher redshifts. Jogee et al. (2004, right-pointing triangles) found a minimal decline in the bar fraction at higher redshifts. Finally, the bar fractions, as found in the Auriga cosmological simulations in Fragkoudi et al. (2020, exes) are shown as thin crosses.

2 (Gadotti et al. 2015), while for NGC 1433, this happened at $z \approx 1$ (de Sá-Freitas et al. 2023). None the less, it is important to point out that not necessarily all barred galaxies observed at $2 < z \leq 3$ will remain as a barred disc galaxy down to $z \approx 0$, as the galaxies in the TIMER sample: late violent mergers may destroy the bar, as well as the disc altogether.

In a recent study conducted by Guo et al. (2023), six strongly barred galaxies were identified at $z > 1$ using rest-frame NIR images from the first four pointings of CEERS. The six observed galaxies have a range in redshift from $z \approx 1.1$ to ≈ 2.3, using photometric redshifts (see Guo et al. 2023; Stefanon et al. 2017). In a cross-check, we find that all barred galaxies identified by Guo et al. were also classified by us as barred.

Several previous studies have found a decline in the fraction of bars in disc and spiral galaxies with redshift, however mass- and volume limits vary between the studies, along with the bar classification method. Sheth et al. (2008) observe the evolution of the bar fraction at redshifts $0.2 < z < 0.84$ from luminous (brighter than $L_V^\star$) face-on spiral galaxies in the COSMOS 2 deg^2 field. The classification methods used in Sheth et al. are ellipse-fitting and visual, which are cross-checked, and an agreement of 85 per cent is found. Masters et al. (2011) found the bar fraction of a volume-limited visually selected SDSS sample using Galaxy Zoo at redshifts $0.01 < z < 0.06$ and $M_r < -19.38$. Melvin et al. (2014) use visually selected galaxies via Galaxy Zoo from COSMOS *HST* images at redshifts $0.4 \leq z \leq 1.0$ with an applied stellar mass limit of $\log(M_\star/\mathrm{M}_\odot) \geq 10$. The bar fraction was extended to redshifts $0.5 \leq z \leq 2.0$ in Simmons et al. (2014) through the visually selected CANDELS galaxies via Galaxy Zoo with an absolute H-band magnitude limit of $H < 25.5$. With the work of Simmons et al. overlapping with the lower redshift bin of our study and using visually identified CANDELS galaxies, we found that our results are in good agreement. Although many studies have found a decrease in the bar fraction at $z = 0$–1, some find little or no evolution of the bar fraction. Jogee et al. (2004) identified bars in spiral galaxies using three independent techniques and found the fraction of bars to be $\sim 30 \pm 6$ per cent in the COSMOS field from the HST Advanced Camera for Surveys (ACS) at redshifts $z \sim 0.2$–0.7 and ~ 0.7–1.0, with completeness cuts of $M_V \leq -19.3$ and -20.6, respectively. Elmegreen et al. (2004) also found a constant bar fraction of $\sim 23 \pm 3$ per cent at redshifts $z \sim 0.0$–1.0 in COSMOS-ACS galaxies.

A direct comparison between the results from these various studies is difficult to accomplish given the different techniques employed to identify bars and the different sample selection criteria. In particular, Erwin (2018) shows that in the local Universe the bar fraction depends strongly on galaxy mass, with a peak at $M_\star \sim 10^{9.7}\,\mathrm{M}_\odot$, declining towards both higher and lower masses. At redshifts $0.2 \leq z \leq 0.6$ for a mass complete sample of $M > 10^{10.5}\mathrm{M}_\odot$ galaxies in the COSMOS field, Cameron et al. (2010) found the bar fraction of early-type discs with intermediate stellar masses to be twice that of late-type discs, and is reversed for high stellar masses. In this context, it is important to highlight that our sample probes the galaxy

population with masses above $\approx 10^9\,M_\odot$, which at redshift zero may reflect the peak in the bar fraction distribution. Considering all barred galaxies we find in our study, their mean stellar mass is $M_\star \sim 1.2 \times 10^{10} M_\odot$, with a standard deviation of $\sim 5.8 \times 10^{10}\,M_\odot$.

With the different redshift ranges and stellar masses probed, as well as rest-frame wavelength ranges, samples and techniques employed to find bars and disc galaxies in the different studies, it is clear that while Fig. 7 presents an interesting summary of the findings from different studies, a direct comparison between these studies must account for a number of effects. One could venture into accounting, for example, for the various mass ranges by assuming a $z = 0$ variation of the bar fraction with mass and translating it to the samples probed at higher redshifts. However, this exercise would have to assume that such variation is constant with redshift, an assertion that has not yet been investigated with enough depth to the best of our knowledge. Moreover, the other effects mentioned may be as important, and recipes to account for those are not straightforward to devise.

Using the magnetic-hydrodynamical cosmological simulation TNG50 (Nelson et al. 2019), Rosas-Guevara et al. (2022) found that $M_\star \geq 10^{10} M_\odot$ spiral galaxies with bar formation are present as early as $z = 4$. When an angular resolution limit of twice the *HST I*-band angular PSF FWHM was applied, the fraction of bars dropped to a tenth of its original value at $z = 2$, reconciling theoretical predictions and observations. The rapid onset of bar formation in massive galaxies at early cosmic times has been predicted in numerical simulations for baryon-dominated systems (see e.g. Algorry et al. 2017; Fragkoudi et al. 2021; Bland-Hawthorn et al. 2023). And, in fact, recent studies have found candidate barred galaxies at higher redshifts than our limit at $z = 3$. Costantin et al. (2023) used *HST* and *JWST* images in multiple filters to study a galaxy at $z \simeq 3$ in the mass range of Milky Way progenitors and found evidence of a bar. Going further in wavelength than what is possible with *JWST*, Tsukui et al. (2023) and Smail et al. (2023) explored the submillimetre domain to find dusty, star-forming galaxies at $z > 4$ with morphology indicative of a bar. If these galaxies are confirmed as barred, they provide strong constraints to cosmological simulations.

Some of the previous observational studies discussed above suggest that the decrease in the bar fraction in massive disc galaxies out to $z \sim 1$ could be due to minor merger events that keep the disc dynamically hot. However, depending on the details of the merger/flyby interaction, this could, in fact, tidally induce bar formation (e.g. Berentzen et al. 2003; Peschken & Łokas 2019).

The decline in the bar fraction in disc galaxies could be explained as a result of the decreasing physical spatial resolution with redshift. The ellipticity of bars at poorer resolution decreases, leading to a rounder, less elongated and compact bar, making the stellar bar less distinguishable. The perceptibility of a bar could be considerably affected by a clumpy outer disc, a bright central bulge and/or the angular size of the bar (e.g. Lee et al. 2019). In the context of our results using *JWST*, the PSF FWHM for the *JWST F444W* filter is 0.145 arcsec. The median redshift for barred galaxies between $1 \leq z \leq 2$ is $z = 1.48$, corresponding to a mean linear resolution of $\approx$1.26 kpc. As for the redshift bin $2 < z \leq 3$, the median redshift of barred galaxies is $z = 2.28$, corresponding to a mean linear resolution of $\approx$1.22 kpc. Bars smaller in angular size could have been preferentially missed at the high redshifts explored in this study. In a volume-limited SDSS galaxy sample where bars were identified through ellipse fits and Fourier analysis, Aguerri et al. (2009) established that only bars with lengths above 2.5 times the FWHM can be identified. The proposal that the high-redshift bar fraction is systematically underestimated was thoroughly discussed in the context of a mass- and volume-limited S^{4}G galaxy sample in Erwin (2018), where visual bar length measurements were obtained from Herrera-Endoqui et al. (2015). Erwin successfully reproduced SDSS bar fraction trends using SDSS observational parameters in simulations on the S^{4}G galaxy sample and suggested a bar length detection limit of $\sim$2 times the FWHM. Applying these detection limits on NIRCam *F444W* images implies that bars shorter than $\sim$2.5–3 kpc in radius (semimajor axis) are missed in our study.

Our resolution limit thus indicates that all bars we detect in this study are longer than $\approx$3 kpc. In fact, Erwin (2005) found that the mean bar semimajor axis is 3.3 kpc for early-type disc galaxies and 1.5 kpc for late-type disc galaxies (see also Gadotti 2011). Therefore, unless the bar size distribution at high redshifts differs from the local distribution, even with *JWST*, we are likely missing a sizeable fraction of barred galaxies (see also the discussion in Liang et al. 2023). In a sample of massive galaxies ($M_\star \geq 10^{10} M_\odot$, $0.02 \leq z \leq 0.07$) studied in Gadotti (2011), there are not many bars that are shorter than 3 kpc (see his Fig. 1) although the author points out that due to resolution limits, he may also miss bars with semimajor axis below 2–3 kpc. However, in Erwin (2005), mass is not presented, so a direct comparison is not straightforward. Erwin (2019), on the other hand, shows that bar length increases with mass for galaxies more massive than $\log(M_\star/M_\odot) \geq 10.1$ for local galaxies, and a substantial fraction of the galaxies in his study has bars shorter than 3 kpc.

Not only absolute bar length but the ratio of bar length to the galaxy size (e.g. disc scale length h, or parameters such as R_{50} or R_{90}) may be more useful to compare at different redshifts, since it has been shown that the galaxy size also evolves (Trujillo et al. 2007; Buitrago et al. 2008, 2014; van der Wel et al. 2014; Whitney et al. 2019, mostly for massive early-type galaxies but also in the case of disc galaxies). Kim et al. (2021) measured bar length for galaxies at $0.2 \leq z \leq 0.84$ and found that the mean length of the bar is $\sim$5 kpc for galaxies with $\log(M_\star/M_\odot) \geq 10$ (see their fig. 2). However, the normalized bar length $R_{\rm bar}/h$ of galaxies at $0.2 \leq z \leq 0.84$ in the study of Kim et al. (2021) is similar to that of local bars in Gadotti (2011). We postpone a thorough discussion on these aspects to a future paper, in which we will also present measurements of the bar length and its evolution at higher redshifts.

It is also interesting to note that the abundance of weakly barred galaxies significantly declines at the higher redshift bin, more so than the abundance of strongly barred galaxies. This suggests the presence of another possible observational bias. While the linear resolution remains similar between $1 \leq z \leq 2$ and $2 \leq z \leq 3$ (as discussed above), cosmological surface brightness dimming is significantly more powerful at the higher redshift bin. This could diminish our ability to see weaker bars, particularly at the higher redshift bin, and this bias could produce a relative drop in the total bar fraction at the higher redshift bin even if the bar fractions in the two redshift bins are in reality comparable.

6 SUMMARY AND CONCLUSIONS

To derive the fraction of stellar bars in disc galaxies at high redshifts is an essential step towards understanding the onset of bar-driven galaxy evolution, which was found in previous studies using rest-frame optical *HST* images to occur at $z \sim 1$. However, stellar bars are populated by evolved stars emitting strongly at longer wavelengths, and thus, bars can be more effectively identified in rest-frame NIR images.

In this study, we observe the evolution of the bar fraction at redshifts $z = 1$–3 in a sample of galaxies present in both *HST* CANDELS and *JWST* CEERS and PRIMER and compare the results obtained after using rest-frame optical *HST* images and rest-frame NIR *JWST* images for galaxies in the same parent sample. We use the longest-wavelength *JWST* NIRCam *F444W* filter to trace the underlying stellar mass distribution as best as possible. The initial parent sample of 1180 galaxies is optimized to produce a sample in which bars can be more robustly identified, in particular by removing galaxies with peculiar morphology and galaxies in a close to edge-on projection, with an inclination limit of $i \leq 60°$. After optimization, the parent sample is reduced to 368 galaxies in the *JWST F444W* filter and 126 galaxies in the *HST F160W* filter. Five co-authors visually classified all galaxies in the two optimized samples, searching for bars supported by radial profiles of isophotal ellipticity and PA.

To observe the evolution of stellar bars in disc galaxies, we used published disc classifications from Ferreira et al. (2023, *JWST* disc classifications) and Kartaltepe et al. (2015, *HST* disc classifications). The fraction of bars in disc galaxies was thus derived for two redshift bins, $1 \leq z \leq 2$ and $2 < z \leq 3$, with robust photometric redshifts and ensuring a mass completeness above 95 per cent. The bar fractions we found in *JWST F444W* are, respectively, $\approx 17.8^{+5.1}_{-4.8}$ per cent and $\approx 13.8^{+6.5}_{-5.8}$ per cent for the lower and higher redshift bins. In *HST F160W*, we found the bar fractions to be $\approx 11.2^{+4.7}_{-3.8}$ per cent and $\approx 6.0^{+8.4}_{-3.7}$ per cent for the lower and higher redshift bins, respectively. Notably, at lower redshifts, we find 20 more barred galaxies in *JWST*, which were not identified in *HST* images and at higher redshifts, we classify nine more galaxies as barred. We thus found the bar fraction to be approximately two times greater in *JWST F444W* than in *HST F160W*, hence the rest-frame NIR bar fractions are twice the optical, showing that the detectability of stellar bars depends significantly on the wavelength range and the sensitivity of the instrument. A decrease in the bar fraction is observed at higher redshifts, but the trend could be due to shorter bars being preferentially missed from this study. We detect a substantial number of barred galaxies at redshifts $z \leq 3$, implying that bar-driven galaxy evolution could commence at least in some galaxies at a lookback time ∼11 Gyr, given that some bar-driven processes, such as promoting gas inflow along the bar leading edges, are thought to proceed quickly after bar formation (∼0.1 Gyr; see e.g. Athanassoula 1992; Seo et al. 2019; Baba & Kawata 2020). In fact, Guo et al. (2023) have recently reported the finding of a barred galaxy at $z \approx 2.3$, and other teams have reported candidate barred galaxies beyond redshift three (Costantin et al. 2023; Amvrosiadis et al. 2024) and even beyond redshift four (Tsukui et al. 2023; Smail et al. 2023). In this study, the highest redshift strongly and weakly barred galaxies found are at $z \simeq 2.3$ and $\simeq 2.8$, respectively.

This study does not extend beyond $z = 3$ to remain in the rest-frame NIR and better detect the evolved stellar populations within the bar. Interesting investigations can be done on the bar fraction dependence on galaxy stellar mass and the evolution of the bar length, which are beyond the scope of this paper but will be explored in future papers. This study used the first four pointing of CEERS, and a future paper will present an enlarged census of the bar fraction at redshifts $1 \leq z \leq 3$ using the remaining six CEERS pointings.

ACKNOWLEDGEMENTS

We thank the anonymous referee for a constructive and timely report. We also thank Peter Erwin for sending useful comments. ZLC acknowledges funding from the Science and Technology Facilities CouncilST/X508354/1. This work was supported by STFC grants ST/T000244/1 and ST/X001075/1. TK acknowledges support from the Basic Science Research Program through the National Research Foundation of Korea (NRF), funded by the Ministry of Education (RS-2023-00240212 and no. 2019R1I1A3A02062242) and the grant funded by the Korean government (MSIT) (no. 2022R1A4A3031306 and WISET 2022-804). JN acknowledges funding from the European Research Council (ERC) under the European Union's Horizon 2020 research and innovation programme (grant agreement no. 694343). EA thanks the CNES for financial support. For the purpose of open access, the authors have applied a Creative Commons Attribution (CC BY) to any Author Accepted Manuscript version arising.

DATA AVAILABILITY

This work used ASTROPY (Astropy Collaboration 2013) and PHOTUTILS (Bradley et al. 2022). The specific observations analysed can be accessed via https://doi.org/10.17909/xm8m-tt59, and the visual classifications from Ferreira et al. (2023) are publicly available at https://github.com/astroferreira/CEERS_EPOCHS_MORPHO/

REFERENCES

Abraham R. G., Merrifield M. R., Ellis R. S., Tanvir N. R., Brinchmann J., 1999, MNRAS, 308, 569
Abraham S., Aniyan A. K., Kembhavi A. K., Philip N. S., Vaghmare K., 2018, MNRAS, 477, 894
Adams N. J. et al., 2023, MNRAS, 518, 4755
Aguerri J. A. L., Méndez-Abreu J., Corsini E. M., 2009, A&A, 495, 491
Algorry D. G. et al., 2017, MNRAS, 469, 1054
Allard E. L., Knapen J. H., Peletier R. F., Sarzi M., 2006, MNRAS, 371, 1087
Alonso M. S., Coldwell G., Lambas D. G., 2013, A&A, 549, A141
Alonso S., Coldwell G., Duplancic F., Mesa V., Lambas D. G., 2018, A&A, 618, A149
Amvrosiadis A. et al., ., 2024, preprint (arXiv:2404.01918)
Astropy Collaboration, 2013, A&A, 558, A33
Athanassoula E., 1992, MNRAS, 259, 345
Athanassoula E., 2005, Celest. Mech. Dyn. Astron., 91, 9
Athanassoula E., Morin S., Wozniak H., Puy D., Pierce M. J., Lombard J., Bosma A., 1990, MNRAS, 245, 130
Athanassoula E., Rodionov S. A., Peschken N., Lambert J. C., 2016, ApJ, 821, 90
Athanassoula L., 2003, Angular Momentum Redistribution and the Evolution and Morphology of Bars. Springer, Berlin, Heidelberg, p. 313
Baba J., Kawata D., 2020, MNRAS, 492, 4500
Barazza F. D. et al., 2009, A&A, 497, 713
Barazza F. D., Jogee S., Marinova I., 2008, ApJ, 675, 1194
Berentzen I., Athanassoula E., Heller C. H., Fricke K. J., 2003, MNRAS, 341, 343
Bittner A. et al., 2020, A&A, 643, A65
Bland-Hawthorn J., Tepper-Garcia T., Agertz O., Freeman K., 2023, ApJ, 947, 80
Bradley L. et al., 2022, astropy/photutils: 1.5.0, doi:10.5281/zenodo.6825092.
Brown L. D., Cai T. T., DasGupta A., 2001, Stat. Sci., 16, 101
Buitrago F., Conselice C. J., Epinat B., Bedregal A. G., Grützbauch R., Weiner B. J., 2014, MNRAS, 439, 1494
Buitrago F., Trujillo I., Conselice C. J., Bouwens R. J., Dickinson M., Yan H., 2008, ApJ, 687, L61
Buta R. J. et al., 2015, ApJS, 217, 32
Buta R., Alpert A. J., Cobb M. L., Crocker D. A., Purcell G. B., 1998, AJ, 116, 1142
Cameron E. et al., 2010, MNRAS, 409, 346
Cameron E., 2011, Publ. Astron. Soc. Aust., 28, 128
Carles C., Martel H., Ellison S. L., Kawata D., 2016, MNRAS, 463, 1074
Cheng T.-Y. et al., 2021, MNRAS, 507, 4425
Cheung E. et al., 2013, ApJ, 779, 162
Cisternas M., Sheth K., Salvato M., Knapen J. H., Civano F., Santini P., 2015, ApJ, 802, 137

Clopper C. J., Pearson E. S., 1934, Biometrika, 26, 404
Coelho P., Gadotti D. A., 2011, ApJ, 743, L13
Combes F., Debbasch F., Friedli D., Pfenniger D., 1990, A&A, 233, 82
Combes F., Sanders R. H., 1981, A&A, 96, 164
Contopoulos G., Grosbol P., 1989, A&AR, 1, 261
Contopoulos G., Papayannopoulos T., 1980, A&A, 92, 33
Costantin L. et al., 2023, Nature, 623, 499
de Lorenzo-Cáceres A., Vazdekis A., Aguerri J. A. L., Corsini E. M., Debattista V. P., 2012, MNRAS, 420, 1092
de Sá-Freitas C. et al., 2023, A&A, 671, A8
de Vaucouleurs G., de Vaucouleurs A., Corwin, Herold G. J., Buta R. J., Paturel G., Fouque P., 1991, Third Reference Catalogue of Bright Galaxies. Springer-Verlag, Berlin
Di Matteo P., Haywood M., Combes F., Semelin B., Snaith O. N., 2013, A&A, 553, A102
Duncan K. et al., 2019, ApJ, 876, 110
Dunlop J. S. et al., 2021, PRIMER: Public Release IMaging for Extragalactic Research. JWST Proposal. Cycle 1, ID. #1837.
Elmegreen B. G., Elmegreen D. M., Hirst A. C., 2004, ApJ, 612, 191
Erwin P., 2005, MNRAS, 364, 283
Erwin P., 2018, MNRAS, 474, 5372
Erwin P., 2019, MNRAS, 489, 3553
Eskridge P. B. et al., 2000, AJ, 119, 536
Ferreira L. et al., 2023, ApJ, 955, 94
Finkelstein S. L. et al., 2023, ApJ, 946, L13
Fragkoudi F. et al., 2020, MNRAS, 494, 5936
Fragkoudi F., Athanassoula E., Bosma A., 2016, MNRAS, 462, L41
Fragkoudi F., Di Matteo P., Haywood M., Schultheis M., Khoperskov S., Gómez A., Combes F., 2018, A&A, 616, A180
Fragkoudi F., Grand R. J. J., Pakmor R., Springel V., White S. D. M., Marinacci F., Gomez F. A., Navarro J. F., 2021, A&A, 650, L16
Frogel J. A., Quillen A. C., Pogge R. W., 1996, in Block D. L., Greenberg J. M., eds, Astrophysics and Space Science Library, Vol. 209, New Extragalactic Perspectives in the New South Africa. Kluwer Academic Publishers, Dordrecht, p. 65
Gadotti D. A. et al., 2019, MNRAS, 482, 506
Gadotti D. A. et al., 2020, A&A, 643, A14
Gadotti D. A., 2011, MNRAS, 415, 3308
Gadotti D. A., Athanassoula E., Carrasco L., Bosma A., de Souza R. E., Recillas E., 2007, MNRAS, 381, 943
Gadotti D. A., Seidel M. K., Sánchez-Blázquez P., Falcón-Barroso J., Husemann B., Coelho P., Pérez I., 2015, A&A, 584, A90
Garland I. L. et al., 2023, MNRAS, 522, 211
Gavazzi G. et al., 2015, A&A, 580, A116
Gelman A., Carlin J., Stern H., Dunson D., Vehtari A., Rubin D., 2003, Bayesian Data Analysis, 2nd edn. Chapman and Hall/CRC, New York
Grogin N. A. et al., 2011, ApJS, 197, 35
Guo Y. et al., 2023, ApJ, 945, L10
Herrera-Endoqui M., Díaz-García S., Laurikainen E., Salo H., 2015, A&A, 582, A86
Hohl F., 1971, ApJ, 168, 343
Huertas-Company M. et al., 2023, preprint (arXiv:2305.02478)
Ishizuki S., Kawabe R., Ishiguro M., Okumura S. K., Morita K.-I., 1990, Nature, 344, 224
Jedrzejewski R. I., 1987, MNRAS, 226, 747
Jogee S. et al., 2004, ApJ, 615, L105
Kalnajs A. J., 1972, ApJ, 175, 63
Kartaltepe J. S. et al., 2015, ApJS, 221, 11
Kim T., Athanassoula E., Sheth K., Bosma A., Park M.-G., Lee Y. H., Ann H. B., 2021, ApJ, 922, 196
Knapen J. H., Beckman J. E., Heller C. H., Shlosman I., de Jong R. S., 1995, ApJ, 454, 623
Koekemoer A. M. et al., 2011, ApJS, 197, 36
Kormendy J., 1982, ApJ, 257, 75
Kormendy J., Kennicutt, Robert C. J., 2004, ARA&A, 42, 603
Kraljic K., Bournaud F., Martig M., 2012, ApJ, 757, 60
Lee Y. H., Ann H. B., Park M.-G., 2019, ApJ, 872, 97
Liang X., Yu S.-Y., Fang T., Ho L. C., 2023, preprint (arXiv:2311.04019)
Lynden-Bell D., Kalnajs A. J., 1972, MNRAS, 157, 1
Marinova I., Jogee S., 2007, ApJ, 659, 1176
Masters K. L. et al., 2011, MNRAS, 411, 2026
Melvin T. et al., 2014, MNRAS, 438, 2882
Méndez-Abreu J., Costantin L., Kruk S., 2023, A&A, 678, A54
Méndez-Delmestre K., Sheth K., Schinnerer E., Jarrett T. H., Scoville N. Z., 2007, ApJ, 657, 790
Nair P. B., Abraham R. G., 2010, ApJ, 714, L260
Nelson D. et al., 2019, Comput. Astrophys. Cosmol., 6, 2
Nelson E. J. et al., 2023, ApJ, 948, L18
Ostriker J. P., Peebles P. J. E., 1973, ApJ, 186, 467
Peschken N., Łokas E. L., 2019, MNRAS, 483, 2721
Planck Collaboration VI, 2020, A&A, 641, A6
Regan M. W. et al., 2006, ApJ, 652, 1112
Rosas-Guevara Y. et al., 2022, MNRAS, 512, 5339
Sakamoto K., Okumura S. K., Ishizuki S., Scoville N. Z., 1999, ApJ, 525, 691
Sanders R. H., Tubbs A. D., 1980, ApJ, 235, 803
Schneider P., 2006, Extragalactic Astronomy and Cosmology. Springer, Berlin, Heidelberg
Sellwood J. A., Wilkinson A., 1993, Rep. Prog. Phys., 56, 173
Seo W.-Y., Kim W.-T., Kwak S., Hsieh P.-Y., Han C., Hopkins P. F., 2019, ApJ, 872, 5
Sheth K. et al., 2008, ApJ, 675, 1141
Sheth K., Regan M. W., Scoville N. Z., Strubbe L. E., 2003, ApJ, 592, L13
Sheth K., Vogel S. N., Regan M. W., Thornley M. D., Teuben P. J., 2005, ApJ, 632, 217
Silva-Lima L. A., Martins L. P., Coelho P. R. T., Gadotti D. A., 2022, A&A, 661, A105
Simmons B. D. et al., 2014, MNRAS, 445, 3466
Smail I. et al., 2023, Hidden giants in JWST's PEARLS: An ultra-massive z = 4.26 sub-millimeter galaxy that is invisible to HST, preprint (arXiv:2306.16039)
Stefanon M. et al., 2017, ApJS, 229, 32
Trujillo I., Conselice C. J., Bundy K., Cooper M. C., Eisenhardt P., Ellis R. S., 2007, MNRAS, 382, 109
Tsukui T., Wisnioski E., Bland-Hawthorn J., Mai Y., Iguchi S., Baba J., Freeman K., 2023, Detecting a disk bending wave in a barred-spiral galaxy at redshift 4.4. preprint (arXiv:2308.14798)
van der Wel A. et al., 2014, ApJ, 788, 28
Wang Y., Athanassoula E., Patsis P., Mao S., 2022, A&A, 668, A55
Weinberg M. D., 1985, MNRAS, 213, 451
Whitney A., Conselice C. J., Bhatawdekar R., Duncan K., 2019, ApJ, 887, 113
Wozniak H., Friedli D., Martinet L., Martin P., Bratschi P., 1995, A&AS, 111, 115
Wright E. L., 2006, PASP, 118, 1711

APPENDIX A: STRONGLY AND WEAKLY BARRED GALAXIES

In this study, we have visually identified CEERS galaxies as strongly barred, weakly barred or unbarred in *JWST* NIRCam *F444W* images between redshifts $1 \leq z \leq 3$. Fig. A1 shows the strongly barred galaxies, while Fig. A2 shows the weakly barred galaxies identified in this study. Table A1 lists the *HST* classifications from Kartaltepe et al. (2015) of all barred galaxies, along with their photometric redshifts and stellar masses from Duncan et al. (2019).

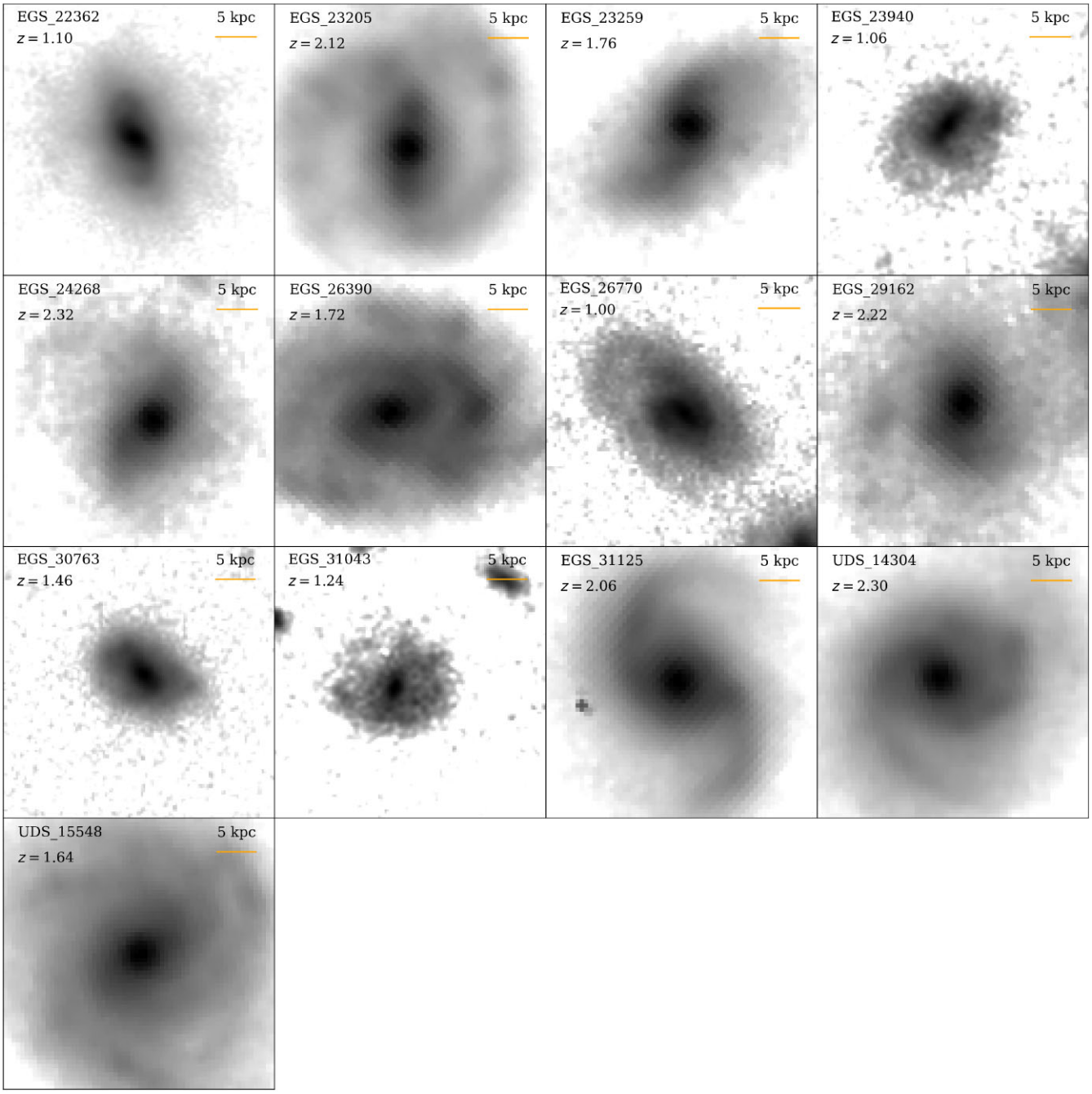

Figure A1. Rest-frame NIR logarithmic images of strongly barred galaxies using the *JWST* NIRCam *F444W* filter between the redshifts $1 \leq z \leq 3$. The redshift of the galaxy is noted in the upper left corner of each image. A 5 kpc scale is given in the upper right corner of each image (calculated using Wright 2006).

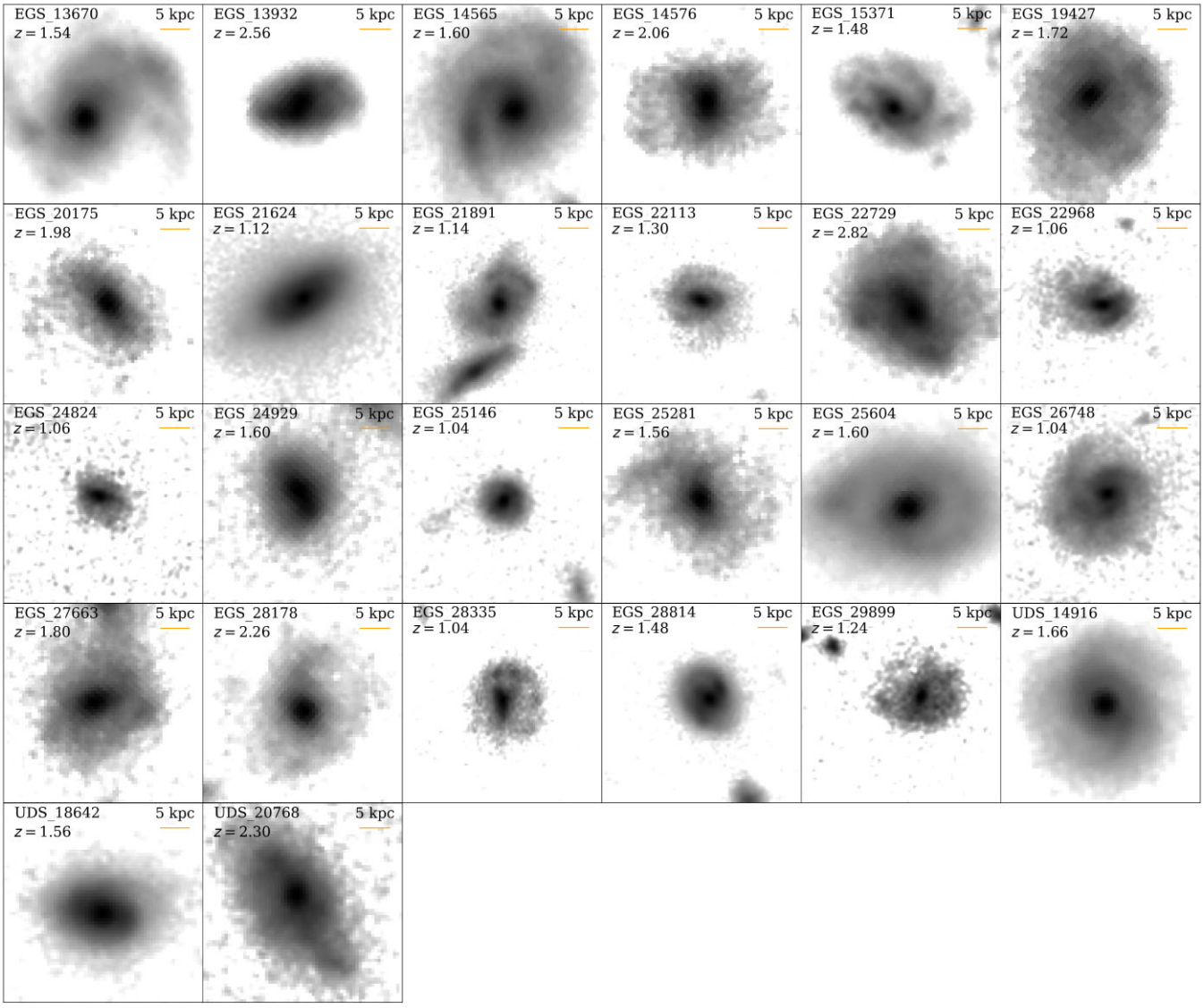

Figure A2. Rest-frame NIR logarithmic images of weakly barred galaxies using the *JWST* NIRCam *F444W* filter between the redshifts $1 \leq z \leq 3$. The redshift of the galaxy is noted in the upper left corner of each image. A 5 kpc scale is given in the upper right corner of each image (calculated using Wright 2006).

Table A1. The 39 visually classified strongly and weakly barred galaxies.

Galaxy ID	z	$\log_{10}(M_\star/M_\odot)$	Bar type	Class
EGS_13670	1.54	10.63	Weak	Face-on barred disc with spiral arms
EGS_13932	2.56	10.61	Weak	Disc
EGS_14565	1.60	10.24	Weak	Barred disc dominated with spiral arms
EGS_14576	2.06	9.53	Weak	Disc
EGS_15371	1.48	10.67	Weak	Asymmetric disc
EGS_19427	1.72	9.95	Weak	Disc with non-interacting companion
EGS_20175	1.98	9.36	Weak	Disc
EGS_21624	1.12	10.65	Weak	Disc-dominated spheroid
EGS_21891	1.14	9.73	Weak	Interacting disc with spiral arms
EGS_22113	1.30	9.75	Weak	Disc
EGS_22362	1.10	10.71	Strong	Spheroidal disc
EGS_22729	2.82	10.23	Weak	Irregular asymmetric disc
EGS_22968	1.06	9.11	Weak	Disc with spiral arms
EGS_23205	2.12	11.20	Strong	Disc
EGS_23259	1.76	10.47	Strong	Interacting asymmetric irregular disc
EGS_23940	1.06	9.70	Strong	Disc with spiral arms and non-interacting companion
EGS_24268	2.32	10.20	Strong	Asymmetric irregular
EGS_24824	1.06	9.03	Weak	Disc
EGS_24929	1.60	9.48	Weak	Asymmetric irregular with non-interacting companion
EGS_25146	1.04	9.27	Weak	Disc with non-interacting companion
EGS_25281	1.56	9.33	Weak	Face-on disc dominated spheroid
EGS_25604	1.60	10.89	Weak	Face-on spheroidal disc
EGS_26390	1.72	10.69	Strong	Face-on asymmetric disc
EGS_26748	1.04	10.08	Weak	Face-on disc
EGS_26770	1.00	9.74	Strong	Interacting face-on disc
EGS_27663	1.80	9.88	Weak	Face-on disc with non-interacting companion
EGS_28178	2.26	10.03	Weak	Face-on asymmetric disc dominated irregular
EGS_28335	1.04	9.33	Weak	Disc with spiral arms
EGS_28814	1.48	10.16	Weak	Asymmetric irregular disc
EGS_29162	2.22	10.04	Strong	Interacting asymmetric irregular
EGS_29899	1.24	8.96	Weak	No classification found
EGS_30763	1.46	10.11	Strong	Asymmetric irregular
EGS_31043	1.24	9.14	Strong	Face-on disc with non-interacting companion
EGS_31125	2.06	11.30	Strong	Face-on disc with spiral arms
UDS_14304	2.30	11.43	Strong	Interacting spheroidal point source
UDS_14916	1.66	10.59	Weak	Face-on disc-dominated spheroid
UDS_15548	1.64	11.18	Strong	Edge-on disc with non-interacting companion
UDS_18642	1.56	10.40	Weak	Asymmetric disc
UDS_20768	2.30	10.07	Weak	Disc

Notes. Column (1): the ID number is from the original SExtractor catalogue based on the full EGS and UDS mosaic. Column (2): CANDELS-based catalogue photometric redshifts (Duncan et al. 2019). Column (3): CANDELS-based catalogue stellar masses (Duncan et al. 2019). Column (4): The classification of bar strength determined from *JWST* NIRCam images. Column (5): *HST* visual classifications from Kartaltepe et al. (2015).

APPENDIX B: IMPACT OF INSTRUMENT SENSITIVITY ON CLASSIFICATIONS

The improved sensitivity and longer wavelength range of *JWST* enhance galaxy images as compared to what was previously seen in *HST* WFC3 images. Fig. B1 shows three galaxies in the *HST* WFC3 *F160W* filter and two *JWST* NIRCam filters, *F356W* and *F444W*. These galaxies are interesting as they received maybe-barred or barred votes in visual classifications of *HST* WFC3 *F160W* (for a description of the method, see Section 3), but unbarred votes from all classifiers in *JWST* NIRCam *F444W*. A PSF artefact (as described in Section 2.1) can be identified in the *JWST* NIRCam images of EGS_27018 but becomes inconspicuous in the *HST* WFC3 image. EGS_22339 is a disc galaxy with spiral features, which could have misled visual classifications in the *HST* WFC3 image, but is clearly unbarred in *JWST* NIRCam images. The only galaxy to receive barred votes in the *HST* WFC3 filter and unbarred votes in *JWST* NIRCam filters is EGS_25879, which is due to the blurring of prominent spiral arms in the *F160W* filter.

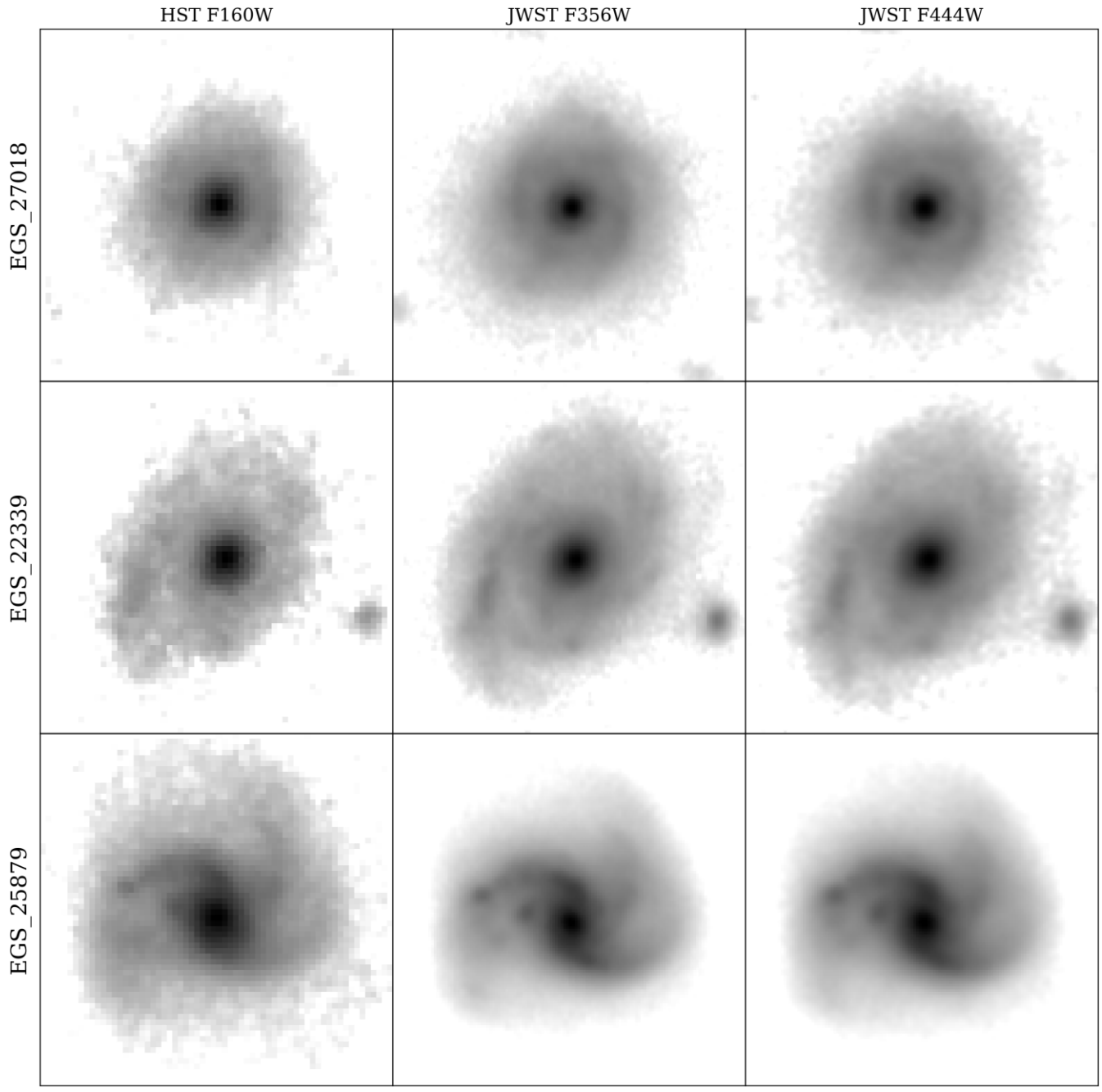

Figure B1. Logarithmic images of the galaxies EGS_27018, EGS_22339 and EGS_25879, which received maybe-barred or barred votes by the classifiers in the *HST* WFC3 *F160W* filter, but unbarred votes in the *JWST* NIRCam *F444W* filter. The three galaxies are shown in the *HST* WFC3 *F160W* (left), *JWST* NIRCam *F356W* (middle), and *JWST* NIRCam *F444W* (right).

This paper has been typeset from a TEX/LATEX file prepared by the author.